(1)

MEASUREMENTS OF LOCAL SKIN FRICTION IN A MICROBUBBLE MODIFIED TURBULENT BOUNDARY LAYER

N. K. Madavan, S. Deutsch and
C. L. Merkle

Technical Memorandum
File No. TM 84-136
24 August 1984
Contract N00014-81-C-0481

Copy No. 2

The Pennsylvania State University
Intercollege Research Programs and Facilities
APPLIED RESEARCH LABORATORY
Post Office Box 30
State College, PA 16801

NAVY DEPARTMENT

OFFICE OF NAVAL RESEARCH

UNCLASSIFIED

SECURITY CLASSIFICATION OF THIS PAGE (When Data Entered)

REPORT DOCUMENTATION PAGE		READ INSTRUCTIONS BEFORE COMPLETING FORM
1. REPORT NUMBER TM 84-136	2. GOVT ACCESSION NO.	3. RECIPIENT'S CATALOG NUMBER
4. TITLE (and Subtitle) MEASUREMENTS OF LOCAL SKIN FRICTION IN A MICROBUBBLE MODIFIED TURBULENT BOUNDARY LAYER		5. TYPE OF REPORT & PERIOD COVERED Technical Memorandum 6. PERFORMING ORG. REPORT NUMBER
7. AUTHOR(s) N. K. Madavan, S. Deutsch and C. L. Merkle		8. CONTRACT OR GRANT NUMBER(s) N00014-81-C-0481
9. PERFORMING ORGANIZATION NAME AND ADDRESS Applied Research Laboratory Post Office Box 30 State College, PA 16804		10. PROGRAM ELEMENT, PROJECT, TASK AREA & WORK UNIT NUMBERS
11. CONTROLLING OFFICE NAME AND ADDRESS Office of Naval Research [Code 432] 800 North Quincy Street Arlington, VA 22217		12. REPORT DATE 24 August 1984 13. NUMBER OF PAGES 56
14. MONITORING AGENCY NAME & ADDRESS (if different from Controlling Office) Naval Sea Systems Command [Code NSEA-63R31] Department of the Navy Washington, DC 20362		15. SECURITY CLASS. (of this report) Unclassified 15a. DECLASSIFICATION DOWNGRADING SCHEDULE

16. DISTRIBUTION STATEMENT (of this Report)

Approved for public release. Distribution unlimited.
Per NAVSEA - 16 October 1984.

17. DISTRIBUTION STATEMENT (of the abstract entered in Block 20, if different from Report)

18. SUPPLEMENTARY NOTES

19. KEY WORDS (Continue on reverse side if necessary and identify by block number)

skin friction
microbubble
turbulent boundary layer

20. ABSTRACT (Continue on reverse side if necessary and identify by block number)

Local skin friction reductions have been measured using an array of flush-mounted hot-film probes in a microbubble-modified, zero pressure gradient, turbulent boundary layer. The results of earlier integrated skin friction measurements, that showed the reduction to be a function of plate orientation, gas flow rate and freestream velocity, have been confirmed both qualitatively and quantitatively. With the measurement

DD FORM 1 JAN 73 1473 EDITION OF 1 NOV 65 IS OBSOLETE

UNCLASSIFIED

SECURITY CLASSIFICATION OF THIS PAGE (When Data Entered)

plate above the boundary layer, it is shown that skin friction is reduced monotonically for all air flow rates at each of three freestream velocities between 4 and 17 m/sec. For the plate below the boundary layer, however, it is possible for increasing gas injection to lead to smaller local skin friction reduction at the lowest speeds. Drag reduction appears to persist for as much as 60-70 boundary layer thicknesses downstream of the injection region. It is further shown, using a probe flush mounted just upstream of the injection section, that there is no apparent upstream interference due to the gas injection. Spectral measurements indicate that microbubbles can cause a reduction of high frequency shear-stress fluctuations. This suggests a destruction of some of the turbulence in the near wall region.

From: N. K. Madavan, S. Deutsch and C. L. Merkle

Subject: Measurements of Local Skin Friction in a Microbubble Modified Turbulent Boundary Layer

Abstract: Local skin friction reductions have been measured using an array of flush-mounted hot-film probes in a microbubble-modified, zero pressure gradient, turbulent boundary layer. The results of earlier integrated skin friction measurements, that showed the reduction to be a function of plate orientation, gas flow rate and freestream velocity, have been confirmed both qualitatively and quantitatively. With the measurement plate above the boundary layer, it is shown that skin friction is reduced monotonically for all air flow rates at each of three freestream velocities between 4 and 17 m/sec. For the plate below the boundary layer, however, it is possible for increasing gas injection to lead to smaller local skin friction reduction at the lowest speeds. Drag reduction appears to persist for as much as 60-70 boundary layer thicknesses downstream of the injection region. It is further shown, using a probe flush mounted just upstream of the injection section, that there is no apparent upstream interference due to the gas injection. Spectral measurements indicate that microbubbles can cause a reduction of high frequency shear-stress fluctuations. This suggests a destruction of some of the turbulence in the near wall region.

I. INTRODUCTION

The authors (Madavan, Deutsch and Merkle 1984a, 1984b; hereafter referred to as MDM1 and MDM2) have recently shown that the introduction of gas bubbles (microbubbles) into a hydrodynamic turbulent boundary layer results in significant reductions in skin friction. In a series of experiments building on some earlier Soviet work (Migirenko and Evseev 1974; Bogdevich and Malyuga 1976; Bogdevich and Evseev 1976), integrated skin friction measurements were made on a 102 mm × 254 mm force balance downstream of a porous injection section. Microbubbles were introduced into the boundary layer by injecting gas (usually air) through the porous surface. The effect of buoyancy, gas flow rate, freestream velocity, gravitational orientation and porous material on the integrated skin friction reduction have been documented in MDM1 and MDM2. Generally speaking, the measurements have shown that the magnitude of the skin friction reduction increases with air flow rate and that it is the ratio of the volumetric flow rate of gas to that of water that is the important parameter. Tests with various types of porous surfaces, including pore size variations over a range of 0.5 to 100 μm, have shown that the skin friction reduction can be realized with a variety of porous materials, although details of the variation of the skin friction reduction with air flow rate are slightly dependent on the type of material.

The microbubble-laden turbulent boundary layer is an extremely complicated flowfield and the mechanisms which lead to the observed skin friction reductions remain unclear. Certainly a proper understanding of the phenomena cannot be expected from integrated skin

friction measurements alone and calls for the measurement of additional details of the flowfield. A more precise knowledge of the microbubble volumetric concentration profiles and bubble size distributions, as well as the modified mean velocity profiles and corresponding turbulence characteristics, are necessary prerequisites for achieving such understanding. This information, however, is very difficult to obtain. First, it is noted that the bubble concentrations of interest are quite high (Migirenko and Evseev 1974 have reported peak concentrations as high as 50 to 80% by volume) so that the microbubble-laden boundary layer is optically opaque, thus precluding the use of contemporary optical measurement techniques. Second, both the earlier reported gravitational effects (MDM1, MDM2) and simple models of the bubble formation process suggest the phenomenon is operative only at high unit Reynolds numbers. Thus, the boundary layers of interest are extremely thin, further aggravating measurement attempts (boundary layer thicknesses are less than 10 mm, while sublayer thicknesses are a few tens of micrometers in the current experiments).

Measurements of bubble concentration profiles reported by Migirenko and Evseev (1974), as well as the authors' own results (MDM1), suggest a bubble-free layer very close to the wall. Local skin friction measurements using flush-mounted hot-film probes become then a practical and attractive first step toward understanding the local characteristics of the microbubble boundary layer. In the current study, an array of flush-mounted hot-film probes has been used to investigate the downstream evolution and persistance of the skin friction reduction. The instantaneous signals

from the hot films have also been utilized to compare the spectral content of the turbulence in the presence and absence of microbubbles.

II. EXPERIMENTAL DETAILS

(a) Facility and Setup

The experiments were conducted in the rectangular test section of the water tunnel facility at The Pennsylvania State University using the boundary layer on the tunnel test section wall. The tunnel is a closed circuit system and the rectangular test section has dimensions of 508 mm × 714 mm × 762 mm long. The flat plate on which the measurements were performed was designed to replace an existing 279 mm × 533 mm long test section window. A 102 mm × 178 mm long porous section for gas injection, followed by a 102 mm × 254 mm force balance was centered spanwise on this test plate (see Fig. 1). Details of the facility used and the experimental setup can be found in MDM1.

An array of six hot-film probes (TSI 1471W) were employed; five of these were flush mounted on the force balance downstream of the injection section, while the sixth probe was mounted immediately upstream. The locations of the probes are shown schematically on Fig. 2. The probes were connected to constant temperature anemometers (both DISA 55M01 and TSI 1750 sets were used). Normally, the probes were operated at an overheat ratio of 1.06, this value being chosen as a compromise between probe sensitivity and probe life.

The porous material used for air injection was of sintered stainless steel, commercially available for use as filter material. Experiments were conducted with the smallest available filter material (0.5 μm), as well as

with a larger size (100 μm). The numbers in parentheses refer to the smallest particle size that can pass through the filter, not the actual pore size.

The tunnel test section velocity was monitored by a transducer that measured the pressure drop across the tunnel contraction section. Injected air flow rate and pressure were measured using a flowmeter and a pressure transducer.

(b) Data Acquisition and Run Procedure

Two methods of data acquisition were used. In the initial experiments, the signals from the six hot films were recorded on three Nicolet digital oscilloscopes and stored on floppy disks. The storage capacity of the disks limited these measurements to 2048 points. These digitized signals were then transferred to an IBM 4341 mainframe system for reduction and analysis. Other flow parameters, namely, tunnel freestream velocity, injected air flow rate and pressure, were taken manually from digital voltmeter readouts at the instant the hot-film signals were recorded. In the latter stages of the experiments, an analog-to-digital (A/D) converter was used to digitize the hot-film signals and feed the data directly to an on-line VAX 11/780 computer. Here, the allowable sample size was much larger. For both methods of data acquisition the sampling rate was typically chosen as 2,000 Hz. The minimum record length used was about 1 second. In both procedures, the data channels were sampled sequentially, the maximum delay between the first and last channel sampled being about 10 μs. The instantaneous voltages from the films were recorded and linearization was accomplished on the computer.

The run procedure used for the local skin friction measurements reported here was as follows. The tunnel velocity was held constant and the air flow rate was set at levels ranging from zero to maximum. At each air flow setting, the oscilloscopes were simultaneously triggered (or sampling was initiated on the A/D converter) to record the hot-film signals. Other flow parameters were recorded at the same time the oscilloscopes were triggered. (With the A/D converter, these parameters were also automatically sampled.) Immediately before and after each run with microbubbles, probe calibration runs were performed by recording the hot-film signals over the range of tunnel velocities in the absence of microbubbles.

(c) The Experimental Boundary Layer

The boundary layer into which microbubbles were introduced was documented by measuring the mean velocity and turbulence intensity profiles and streamwise pressure gradient in the tunnel test section. Details can be found in MDM1, but for the sake of completeness and the important role these data play in hot film probe calibration, the major results are highlighted here.

Mean velocity profiles were obtained at three streamwise locations (shown in Fig. 2) and at two different tunnel speeds (4.7 and 10.6 m/s) using a Laser Doppler Anemometer (LDA). These results are presented in wall variables in Fig. 3, taken from MDM1. The friction velocity used in the figure was evaluated by fitting the near-wall data to Coles (1968) law of the wall. The boundary layer was checked for "full development" by examining the velocity profiles in outer variables, following Purtell et al. (1981). This is shown in Fig. 4, also taken from MDM1. Similarity in the profiles is noted at both tunnel speeds. These velocity measurements, along with measurements of

the pressure gradient along the tunnel test section (see MDM1), establish the experimental boundary layer as being reasonably close to a classical, fully developed, zero pressure gradient turbulent boundary layer.

The calibration procedure adopted here for the hot films (as discussed below) necessitated establishing a virtual origin for the experimental boundary layer. This was accomplished using the boundary layer displacement and momentum thicknesses (δ^* and θ), evaluated from the mean velocity profiles discussed above. Since, for a flat plate turbulent boundary layer, both δ^* and θ are proportional to the distance from the virtual origin to the 0.8 power (4/5), the latter can be linearly extrapolated from a plot of $\delta^{*5/4}$ and $\theta^{5/4}$ versus streamwise distance (referenced to a known location along the boundary layer). By this procedure, the location of the virtual origin was established 180 mm upstream of the porous injection section, as shown in Fig. 5.

(d) Skin Friction Probe Calibration Procedure

Flush-mounted hot-film probes relate the heat transfer rate from the film to the fluid shear stress at the wall. For constant temperature operation of the film, this relationship between the instantaneous voltage output by the anemometer, E (which is directly related to the electrical heat dissipated by the film), and the instantaneous shear stress, τ_w, is of the form,

$$\tau_w^{1/3} = AE^2 + B \quad . \tag{1}$$

Here A and B are constants that must be determined by a calibration procedure in a flow where the shear stress is known either from theory or an independent measurement. Brown (1967), Liepmann and Skinner (1954), and others have suggested that the constants, A and B, determined from a calibration in a

laminar flow can be used for measurement in a turbulent flow. The validity of such a procedure has, however, been questioned (see, for example, Bellhouse and Schultz 1966; Bradshaw and Gregory 1961), since the response of the hot film in a turbulent flow is not necessarily identical to that in a laminar flow with the same shear stress. Moreover, it is difficult to obtain a laminar flow for the calibration experiment, especially one that can cover the range of shear stress values expected in an actual turbulent flow application (Ramaprian and Tu 1983). This is particularly true for the high unit Reynolds number boundary layers of interest here.

In the present study, an in-situ calibration procedure based upon the verified characteristics of the flat plate turbulent boundary layer was used. This was accomplished by recording the voltage signals from each probe at a series of different tunnel freestream velocities in the absence of micro-bubbles. Each signal record was digitized and stored and the time-averaged voltage $\bar{E}$ was computed. The mean local skin friction value $\bar{\tau}_w$ at each probe location and each tunnel velocity was then obtained from classical turbulent boundary layer correlations of skin friction and length Reynolds number, using the virtual origin established from the LDA measurements of the velocity profiles. The use of the classical correlation is justified by the velocity profile measurements that indicate the present boundary layer is a zero pressure gradient turbulent boundary layer. The specific correlation used as the one suggested by White (1974),

$$\bar{\tau}_w = (1/2\rho U_\infty^2) \frac{0.455}{\ln^2(0.06\ Re_x)} \qquad (2)$$

where ρ is the density of water and Re_x the Reynolds number based on the streamwise length, x, measured from the virtual origin to the probe location.

It is worth noting that at these Reynolds numbers (roughly 2 to 10 million), a 10% measurement error in virtual origin will result in no more than a 1% discrepancy in local shear stress.

Having obtained this tabular set of mean voltages and corresponding values of skin friction, the calibration constants A and B in Eq. (1) are evaluated by an iterative technique. In this procedure, A and B are initially approximated by fitting Eq. (1) to the time-averaged tabular data. These values are then iteratively improved by the method described by Sandborn (1979a;1979b) and Hanratty and Campbell (1982). In the present study, one iteration was found sufficient. Two calibration curves were fitted to the data, one at low and the other at high velocities. A typical calibration curve is shown in Fig. 6.

It should be emphasized here that the calibration measurements were made immediately prior to and after measurements with air injection (see Fig. 6). The average of these two calibrations was used for reducing the hot-film data in the presence of microbubbles. In cases where the pre- and post-calibration showed deviations which resulted in the correlation coefficient of the linear least-squares fit to the data being less than 0.95, the entire data set was discarded.

For the case when there are no bubbles in the boundary layer a measure of the validity of the hot-film technique can be obtained by comparing the rms intensity of the skin friction fluctuations, τ_w', measured here to those reported in the literature. Mitchell and Hanratty (1966) and Sirkar and Hanratty (1970) report values of $\tau_w'/\bar{\tau}_w$ ranging between 0.32-0.36 as obtained from electrochemical shear stress measurements. Eckelmann's (1974) measurements in the thick viscous sublayer of a glycerine boundary layer

using a flush-mounted hot film provide a value of 0.24. By assuming that very near the wall $(0 \leq y^+ \lesssim 0.1)$ both the streamwise velocity fluctuations u' and the mean velocity $\bar{U}$ vanish linearly with decreasing distance from the wall, Eckelmann noted that the value of 0.24 was in agreement with the asymptotic slope of Laufer's (1950) measurements of $u'/\bar{U}$.

The measured value of $\tau'/\bar{\tau}_w$ in the absence of microbubbles are compared with the 0.24 value in Fig. 7 for the tunnel velocity range tested. The data were typically scattered around the value 0.2. The agreement with earlier results seems quite reasonable, particularly when one considers the difficulty in obtaining results at the high unit Reynolds numbers and thin sublayers encountered in this study.

III. RESULTS AND DISCUSSION

Experiments were conducted at tunnel freestream velocities ranging between 4 and 17 m/s. For the most part, the porous section fabricated from the smallest available filter material (0.5 μm) was used. Additional experiments were also conducted using the 100 μm porous material. Air flow rates ranged up to 0.006 m^3/s. As is shown later, this flow rate corresponds to a volumetric fraction in the boundary layer of about 0.5, assuming that all of the air flow remains in the boundary layer, which may not be the case.

The local skin friction measurements with microbubbles reported here are presented in terms of the skin friction coefficient, C_f', normalized to the corresponding skin friction coefficient without microbubbles, C_{f_0}', as a function of the volumetric fraction of air in the boundary layer. The air

flow fraction was defined as the volumetric flow rate of air divided by the total flow in the boundary layer

$$\frac{Q_a}{Q_a + Q_w} \tag{3}$$

where

$$Q_w \equiv U_\infty (\delta - \delta^*) b \quad , \tag{4}$$

and the subscripts a and w denote air and water. The boundary layer thickness and displacement thickness, δ and δ^*, are obtained from classical correlations (see White 1974). These thicknesses were calculated at the mid-point of the porous section (in the absence of microbubbles). The parameter b is the width of the porous section.

(a) Plate Below the Boundary Layer

The local skin friction measurements at the various hot-film probe locations with the plate below the boundary layer are shown in Figs. 8 through 10. Note that this orientation (referred to as plate on bottom on the figures), corresponds to the view shown in Fig. 1, where the experimental setup is mounted on the bottom wall of the tunnel. The measurements shown in Fig. 8 are for a tunnel velocity, U_∞ = 16.7 m/s, while those in Figs. 9 and 10 correspond to U_∞ = 10.8 m/s and U_∞ = 4.6 m/s, respectively. The figures represent measurements using the 0.5 μm porous section. Skin friction reductions are noted at all tunnel velocities, but the characteristic trends with volume fraction depend upon U_∞. The reductions are greatest in the region close to the porous section (probes 2 and 3); farther downstream, the skin friction relaxes back toward its undisturbed (no microbubbles) value (probe 6). This is probably due to the decreasing

air content in the boundary layer resulting from both boundary layer growth and bubble migration. At the high and intermediate tunnel velocities (see Figs. 8 and 9), the decrease in skin friction is seen to be monotonic with increasing air flow except possibly for probes 5 and 6 at low air flows.

In contrast to these high and intermediate velocity results, the low velocity results in Fig. 10 show that the skin friction goes through a minimum and then increases with increasing air flow. This indicates an optimum air flow rate for maximum skin friction reduction at low velocities. Based on the results of Silberman (1957) and Hughes et al. (1979) that indicate the bubble diameter is proportional to the square root of the ratio Q_a/U_∞, one can speculate that the reason for this reduced effectiveness of the bubbles at high air flow rates and low velocities may be due to the larger bubble sizes. These larger bubbles quickly migrate out of the boundary layer with this plate orientation, reducing their effectiveness. The same effect was not observed at the high velocities, apparently because of the shorter convection time.

(b) Plate Above the Boundary Layer

The entire test section of the water tunnel can be rotated through 180 degrees, thus effectively positioning the experimental setup on the upper wall of the tunnel. At this orientation, the plate is above the boundary layer (referred to as plate on top in the figures) and the forces due to gravity act to keep the bubbles in the boundary layer. Earlier reported force balance measurements (MDM1) showed substantially higher reductions in the integrated skin friction at this orientation, especially at the lower velocities. The hot film measurements are shown in Figs. 11 through 13 and compared to the measurements with the plate below the boundary layer for a

range of tunnel velocities. Figure 11 compares measurements at U_∞ = 16.8 m/s for the two plate orientations at probe 3 and probe 6 (note that probe 3 is located close to the injection section and probe 6 is located farthest downstream). While the skin friction reductions at probe 3 are of the same magnitude, slightly larger reductions are noted at the downstream probe location when the plate is above the boundary layer. Figure 12 is a similar plot at U_∞ = 10.7 m/s and compares the measurements for the two orientations at probe 2 and probe 6. Once again, it is noted that close to the injection section, the skin friction reductions are independent of gravitational orientation, while farther downstream the plate-on-top orientation again results in somewhat larger C_f' reductions. These increased reductions with the plate on top occur because the bubbles remain longer in the boundary layer where they are most effective. Figure 13 presents additional data for a tunnel velocity at 4.6 m/s. Note that data for probe 6 with the plate above the boundary layer are not available. Quantitative comparison between the two orientations in Fig. 13 is difficult because the maximum air flow rates shown with the plate above the boundary layer are quite small. The fluctuations in the hot-film signals at higher air flow rates were very high and, due to the resulting lack of confidence in the measurments, these results are not presented. The data, however, suggested that the skin friction reductions with increasing air flow were monotonic, as compared to the plate-on-bottom orientation where a definite "bucket" in the curves was noted. These trends seem reasonable when one notes that the maximum integrated skin friction reductions reported in MDM1 were observed at this velocity, (U_∞ = 4.6 m/s) with the plate above the boundary layer.

(c) Effect of Pore Size Variations

The size of the microbubbles is certainly an important parameter in the skin friction reduction. Although both the Soviet results (Bogdevich and Evseev 1976) and intuition suggest that the pore size would be an important variable, literature (Silberman 1957; Hughes et al. 1979) on bubble sizes in turbulent shear flows, though sparse, indicates that the bubble size is not determined primarily by the size of the pores used for injection, but by the characteristics of the flow. To investigate this, two widely different pore sizes, 0.5 μm and 100 μm, were used for gas injection to compare the magnitude of the skin friction reductions. Figures 14 and 15 compare measurements made using the 100 μm and 0.5 μm porous materials for the plate below the boundary layer. Figure 14 compares data at probes 2 and 6 at U_∞ = 16.8 m/s. At U_∞ = 10.7 m/s a direct comparison is not available and for clarity, Fig. 15 presents only the results of the closest (probe 2) and the farthest (probe 6) locations for the 0.5 μm porous section (presented earlier in Fig. 9). These data show that injection pore size does not have a substantial effect on the skin friction results for the conditions tested here. This observation is in agreement with the integrated skin friction measurements reported earlier in MDM2. These results are of some practical importance since with the larger pore size material much less energy need be expended to introduce a given quantity of microbubbles.

(d) Persistence of the Skin Friction Reduction Phenomenon

The downstream distances to which the skin friction reductions persist was studied by cross-plotting the data reported above in terms of a non-dimensional length corrdinate, x/δ, at selected air flow rates. Here x is the downstream distance measured from the trailing edge of the porous

section and δ denotes the undisturbed boundary layer thickness at this location. These results are shown in Figs. 16 through 19. The figures have been reconstructed from mean lines drawn through C_f'/C_{fo}' versus Q_a data. Figures 16 and 17 are for the plate below the boundary layer, at U_∞ = 16.7 m/s and 10.7 m/s. At both velocities, at low air flow rates, the skin friction returns to almost its undisturbed value at the downstream probe location (roughly 35δ). At higher air flow rates, the skin friction reductions are still significant at this location.

Figures 18 and 19 compare the plate above the boundary layer with the plate below the boundary layer data at U_∞ = 16.8 m/s and 10.8 m/s, respectively. The persistence is clearly a function of the gravitational orientation and the tunnel velocity. The slope of the curves is less steep when the plate is above the boundary layer. Extrapolation would indicate that the reductions persist even to 60-70δ. This increased effectiveness is in keeping with other observations.

(e) Upstream Effects due to Introducing Microbubbles in the Flow

In order to check for possible upstream effects of introducing microbubbles into the boundary layer, an additional hot film (probe 1) was mounted 10 mm upstream of the porous injection section. Skin friction measurements at this location are shown in Fig. 20 as a function of the air flow rate for several different test runs. The skin friction remains unchanged with air flow, within the scatter of the data, showing that the introduction of microbubbles into the flow is not felt upstream over the range of velocities presented here.

(f) Comparison of Hot Film and Force Balance Measurements

The local skin friction measurements from the array of hot films can be integrated and compared to the force balance results reported in MDM1. The integrations were carried out by subdividing the measurement section into discrete (nonuniform) intervals around each probe location and assuming the skin friction at each section was represented by the measurement at the corresponding probe. Other integration procedures are possible but yield quantitatively similar results (Madavan 1984). The comparisons are shown in Fig. 21 for different tunnel velocities, plate orientations and porous sections. Excellent agreement is noted between the hot films and the force balance measurements. In all cases the maximum discrepancy between the two is less than 10%. This agreement between two measurement techniques that are based on completely different physical principles provides substantiation for both.

(g) Spectral Analysis of Hot Film Signals

The effect of microbubbles on the near wall turbulence structure was studied by extracting frequency information from the hot-film signals. A typical power spectral density function, W(f), defined by the equation

$$\tau_w' = \int_0^\infty W(f)df \quad , \tag{5}$$

where f is the frequency in cycles per second, is presented in inner variables for no air injection in Fig. 22. The data is from probe 2 and the plate is on the bottom; the different symbols represent various velocities ranging between 4.0 and 17.0 m/sec. The collapse of the data is quite good.

The influence of the microbubbles may be most strikingly observed by considering a sequence of hot-film signal traces comprising a typical run (probe 3, 16.8 m/sec, plate on bottom) as shown in Fig. 23. The traces have been redrawn from the digitized, linearized signals as processed by the computer. The drop in the mean level of skin friction as the air flow rate is increased from zero is clearly seen with reference to a fixed skin friction value, τ_{ref}. In the presence of microbubbles, the hot-film signals exhibit a reduced amount of high frequency content and the turbulence energy appears to shift toward lower frequencies.

In Figs. 24 and 25 the power spectral density functions with microbubbles for probe 2 at a free stream speed of 10.7 m/sec are shown in inner variables. Figure 24 is for the plate below the boundary layer while Fig. 25 is for the plate above. Note that u_τ and τ'_w used in these normalizations are the values with air injection, so that the loss of high frequency signal is masked by the scaling. The inner variable scaling thus remains effective for the microbubble boundary layer. Similar results are observed at higher speeds as shown in Fig. 26. These correspond to the signal traces previously presented in Fig. 23 (probe 3, 16.8 m/sec, plate on bottom).

The power spectral density functions indicate, by the success of inner variable scaling, that the introduction of air causes no major restructuring of the turbulent boundary layer. We note that there is a strong similarity between the results presented here and those obtained in the polymer flow of Fortuna and Hanratty (1972). Apparently there are some similarities in the drag reduction mechanisms for polymers and microbubbles.

IV. CONCLUDING REMARKS

An array of flush-mounted hot films has been used to study the downstream evolution and persistence of the skin friction reduction in the microbubble-laden turbulent boundary layer. The measurements with the hot films are in excellent agreement with earlier reported integrated skin friction measurements obtained using a force balance. The downstream persistence of the skin friction reduction beyond the location of microbubble injection is a function of the gravitational orientation of the plate and the freestream velocity. For the plate above, the boundary layer substantial skin friction reduction persist for some 35δ for low air flow rates and up to 60-70δ for high air flows. The reductions persist for somewhat shorter distances, roughly 50δ, for the plate below the boundary layer.

Contrary to earlier Soviet results, injection pore size was found to have no major effect on the amount of skin friction reduction. A hot-film probe located 10 mm upstream of the porous injection section indicates that gas injection causes no significant upstream influence for the range of freestream speeds tested.

Spectral measurements indicate a clear loss of high frequency signal with air injection. Inner variable scaling of the spectra with u_τ and τ_w', however, seems as effective with microbubbles as without. This indicates that the major effect of the microbubbles in the turbulent boundary layer may be to alter the local effective viscosity and density of the fluid, thus changing the local turbulent Reynolds number, rather than introducing a major restructuring of the turbulence.

ACKNOWLEDGMENT

This work was sponsored by the Office of Naval Research under Contract No. N00024-81-K-0481.

REFERENCES

Bellhouse, B. J. and Schultz, D. L. 1966. Determination of Mean and Dynamic Skin Friction, Separation and Transition in Low Speed Flow with a Thin Film Heated Element. J. Fluid Mech. 24, p. 379.

Bogdevich, V. G. and Evseev, A. R. 1976. Effect of Gas Saturation on Wall Turbulence. In Investigations of Boundary Layer Control (in Russian) (eds. S. S. Kutateladze and G. S. Migirenko), p. 49. Thermophysics Institute Publishing House.

Bogdevich, V. G. and Malyaga, A. G. 1976. The Distribution of Skin Friction in a Turbulent Boundary Layer of Water beyond the Location of Gas Injection. In Investigations of Boundary Layer Control (in Russian) (eds. S. S. Kutateladze and G. S. Migirenko), p. 62. Thermophysics Institute Publishing House.

Bradshaw, P. and Gregory, N. 1961. The Determination of Local Turbulent Skin Friction from Observations in the Viscous Sublayer. Aero. Res. Counc. R. & M. 3202.

Brown, G. L. 1967. Theory and Application of Heated Films for Skin Friction Measurements. Proc. 1967 Heat Transfer and Fluid Mech. Inst. p. 361. Stanford University Press.

Coles, D. E. 1968. The Young Person's Guide to the Data. Proc. AFOSR-IFP Stanford Conference on Computation of Turbulent Boundary Layers. (eds. D. E. Coles and E. A. Hirst). Stanford University Press.

Eckelmann, H. 1974. The Structure of the Viscous Sublayer and the Adjacent Wall Region in a Turbulent Channel Flow. J. Fluid Mech. 65, p. 439.

Fortuna, G. and Hanratty, T. J. 1972. The Influence of Drag-Reducing Polymers on Turbulence in the Viscous Sublayer. J. Fluid Mech. 53, p. 575.

Hanratty, T. J. and Campbell, J. A. 1982. Measurement of Wall Shear Stress. In Fluid Mechanics Measurements (ed. R. J. Goldstein). Hemisphere Publishing Corporation.

Hughes, N. H., Reischmann, M. M. and Holzmann, J. M. 1979. Digital Image Analysis of Two Phase Flow Data. 6th Bienn. Symp. on Turbulence, University of Missouri, Rolla.

Laufer, J. 1950. Investigation of Turbulent Flow in a Two Dimensional Channel. NACA Rept. TN 2123.

Liepmann, H. and Skinner, G. 1954. Shearing-Stress Measurements by Use of a Heated Element. NACA TN 3268.

Madavan, N. K., Deutsch, S. and Merkle, C. L. 1984a. Reduction of Turbulent Skin Friction by Microbubbles. Phys. Fluids 27, p. 356.

Madavan, N. K., Deutsch, S. and Merkle, C. L. 1984b. The Effect of Porous Material on Microbubble Skin Friction Reduction. AIAA Paper 84-0348.

Madavan, N. K. 1984. The Effects of Microbubbles on Turbulent Boundary Layer Skin Friction. Ph.D. Thesis, Dept. of Mech. Engr., The Pennsylvania State University.

Migirenko, G. S. and Evseev, A. R. 1974. Turbulent Boundary Layer with Gas Saturation. Problems of Thermophysics and Physical Hydrodynamics (in Russian). Novosibirsk, Nauka.

Mitchell, J. E. and Hanratty, T. J. 1966. A Study of Turbulence at a Wall using an Electrochemical Wall Shear Stress Meter. J. Fluid Mech. 26, p. 199.

Purtell, L. P., Klebanoff, P. S. and Buckley, F. T. 1981. Turbulent Boundary Layer at Low Reynolds Number. Phys. Fluids 24, p. 802.

Ramaprian, B. R. and Tu, S. W. 1983. Calibration of a Heat Flux Gage for Skin Friction Measurement. J. Fluids Engr. 104, p. 455.

Sandborn, V. A. 1979a. Surface Shear Stress Fluctuations in Turbulent Boundary Layers. Second Symposium on Turbulent Shear Flows. Imperial College, London, p. 361.

Sandborn, V. A. 1979b. Evaluation of the Time Dependent Surface Shear Stress in Turbulent Flows. ASME Preprint 79-WA/FE-17.

Silberman, E. 1957. Production of Bubbles by the Disintegration of Gas Jets in Liquid. Proc. 5th Midwestern Conf. on Fluid Mech., University of Michigan, p. 263.

Sirkar, K. K. and Hanratty, T. J. 1970. The Limiting Behavior of the Turbulent Transverse Velocity Component Close to a Wall. J. Fluids Mech. 44, p. 589.

White, F. M. 1974. Viscous Fluid Flow. McGraw-Hill Publishing Co.

FIGURE CAPTIONS

Figure 1. Schematic of an experimental setup.

Figure 2. Schematic showing hot film probe locations and LDA measurement stations.

Figure 3. LDA velocity profile measurements in the undisturbed boundary layer presented in inner variables [Note shifted origins].

Figure 4. LDA velocity profile measurements in the undisturbed boundary layer presented in outer variables [Note shifted origins].

Figure 5. Determination of the virtual origin.

Figure 6. A typical calibration curve for the flush-mounted hot film probes.

Figure 7. Hot-film measurements of the skin friction fluctuations in the undisturbed boundary layer. The Reynolds number is based on the distance of the respective probe from the virtual origin.

Figure 8. Hot-film measurements of the local skin friction with micro-bubbles as a function of the air flow rate when the plate is below the boundary layer. U_∞ = 16.7 m/s.

Figure 9. Hot-film measurements of the local skin friction with micro-bubbles as a function of the air flow rate when the plate is below the boundary layer. U_∞ = 10.8 m/s.

Figure 10. Hot-film measurements of the local skin friction with micro-bubbles as a function of the air flow rate when the plate is below the boundary layer. U_∞ = 4.6 m/s.

Figure 11. The effect of gravity on the hot-film measurements of the local skin friction with microbubbles. Comparison of data taken with the plate above and below the boundary layer. U_∞ = 16.8 m/s.

Figure 12. The effect of gravity on the hot-film measurements of the local skin friction with microbubbles. Comparison of data taken with the plate above and below the boundary layer. U_∞ = 10.7 m/s.

Figure 13. The effect of gravity on the hot-film measurements of the local skin friction with microbubbles. Comparison of data taken with the plate above and below the boundary layer. U_∞ = 4.6 m/s.

Figure 14. The effect of pore size variations on the local skin friction measurements. Comparison of data taken with the 0.5 μm and 100 μm porous sections. U_∞ = 16.8 m/s.

Figure 15. The effect of pore size variations on the local skin friction measurements. Comparison of data taken with the 0.5 μm and 100 μm porous sections. U_∞ = 10.7 m/s.

Figure 16. The downstream persistence of the skin friction reduction. The plate is below the boundary layer. U_∞ = 16.7 m/s.

Figure 17. The downstream persistence of the skin friction reduction. The plate is below the boundary layer. U_∞ = 10.8 m/s.

Figure 18. The downstream persistence of the skin friction reduction. Comparison of data taken with the plate above and below the boundary layer. U_∞ = 16.8 m/s.

Figure 19. The downstream persistence of the skin friction reduction. Comparison of data taken with the plate above and below the boundary layer. U_∞ = 10.7 m/s.

Figure 20. Hot-film measurements of the local skin friction upstream of microbubble introduction into the boundary layer [Note shifted origins].

Figure 21. Comparison of the integrated skin friction reductions with microbubbles measured by the force balance with that evaluated from the hot films.

Figure 22. Normalized power spectral density functions of the hot-film signals in the presence and absence of microbubbles.

Figure 23. A sequence of linearized hot-film signal traces in the presence and absence of microbubbles.

A: no microbubbles;

B: 10% air, 5% C_f reduction;

C: 14% air, 15% C_f reduction;

D: 19% air, 28% C_f reduction;

E: 26% air, 40% C_f reduction; and

F: 36% air, 62% C_f reduction.

Figure 24. Normalized power spectral density functions of the hot-film signal in the presence of microbubbles. (probe 2, plate on top, 10.7 m/sec).

Figure 25. Normalized power spectral density functions of the hot-film signal in the presence of microbubbles. (probe 2, plate on bottom, 10.7 m/sec).

Figure 26. Normalized power spectral density functions of the hot-film signal in the presence of microbubbles. (probe 3, plate on bottom, 16.8 m/sec).

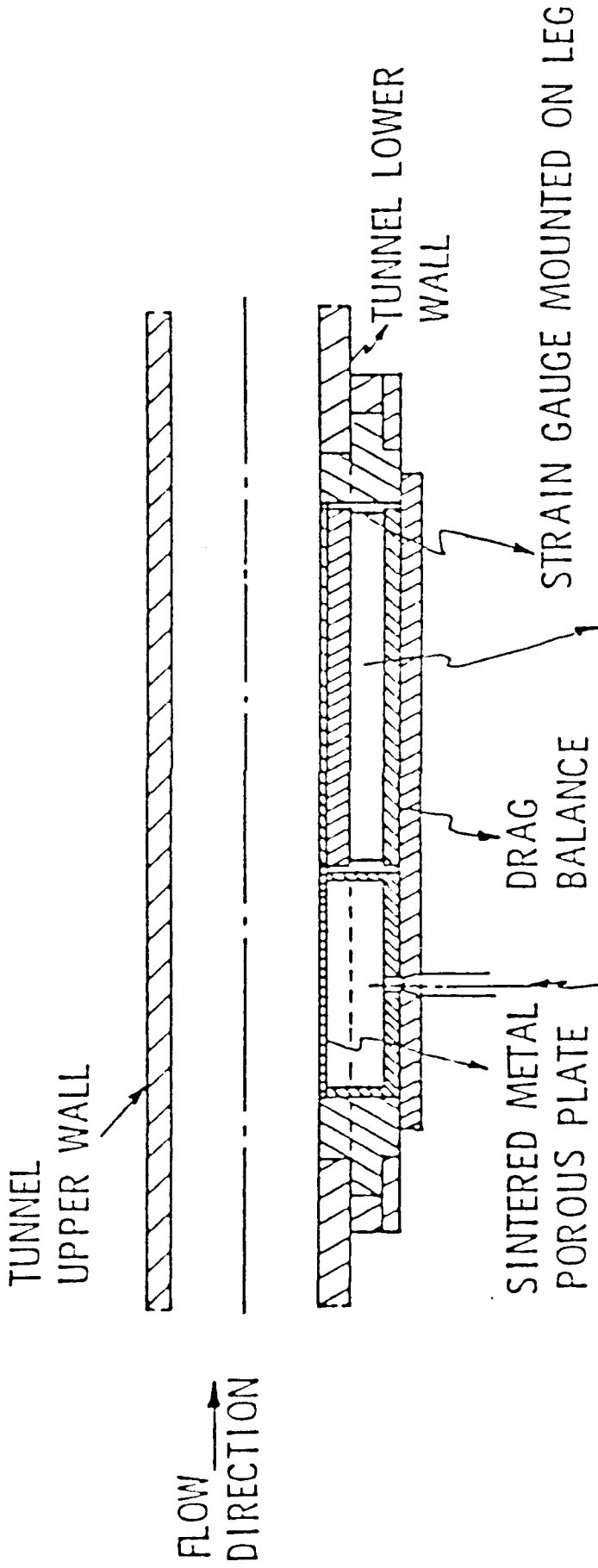

Figure 1. Schematic of an experimental setup.

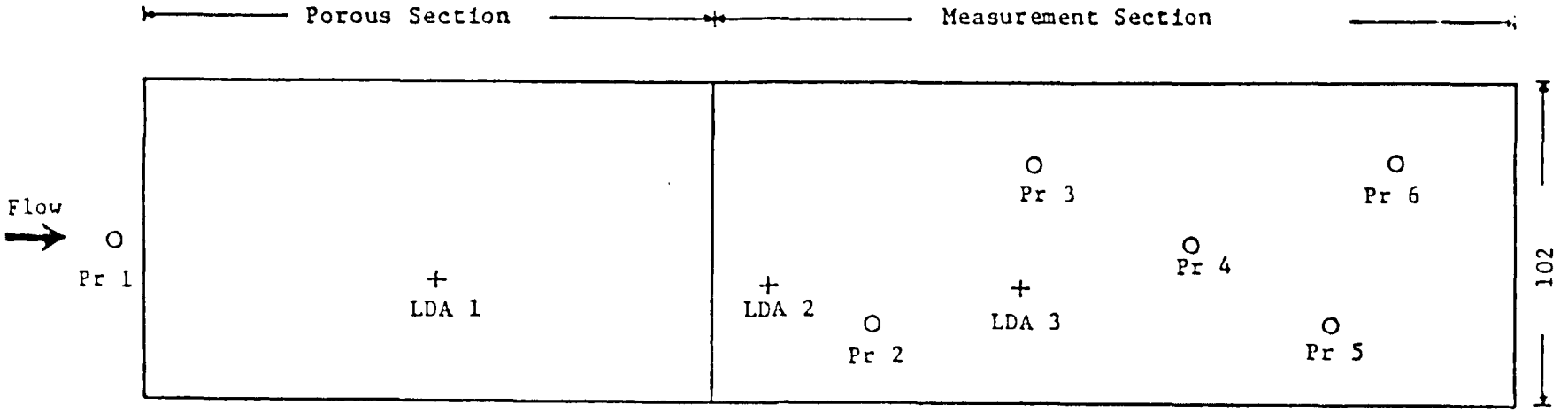

Pr - denotes flush-mounted hot film probe location
LDA - denotes LDA measurement station

	Distance to virtual origin, mm	Distance to leading edge of porous section, mm
Pr 1	170	-10
Pr 2	409	229
Pr 3	460	280
Pr 4	511	331
Pr 5	555	375
Pr 6	575	395
LDA 1	272	92
LDA 2	374	194
LDA 3	454	274

Figure 2. Schematic showing hot film probe locations and LDA measurement stations.

24 August 1984
NKM:SD:CLM:lhz

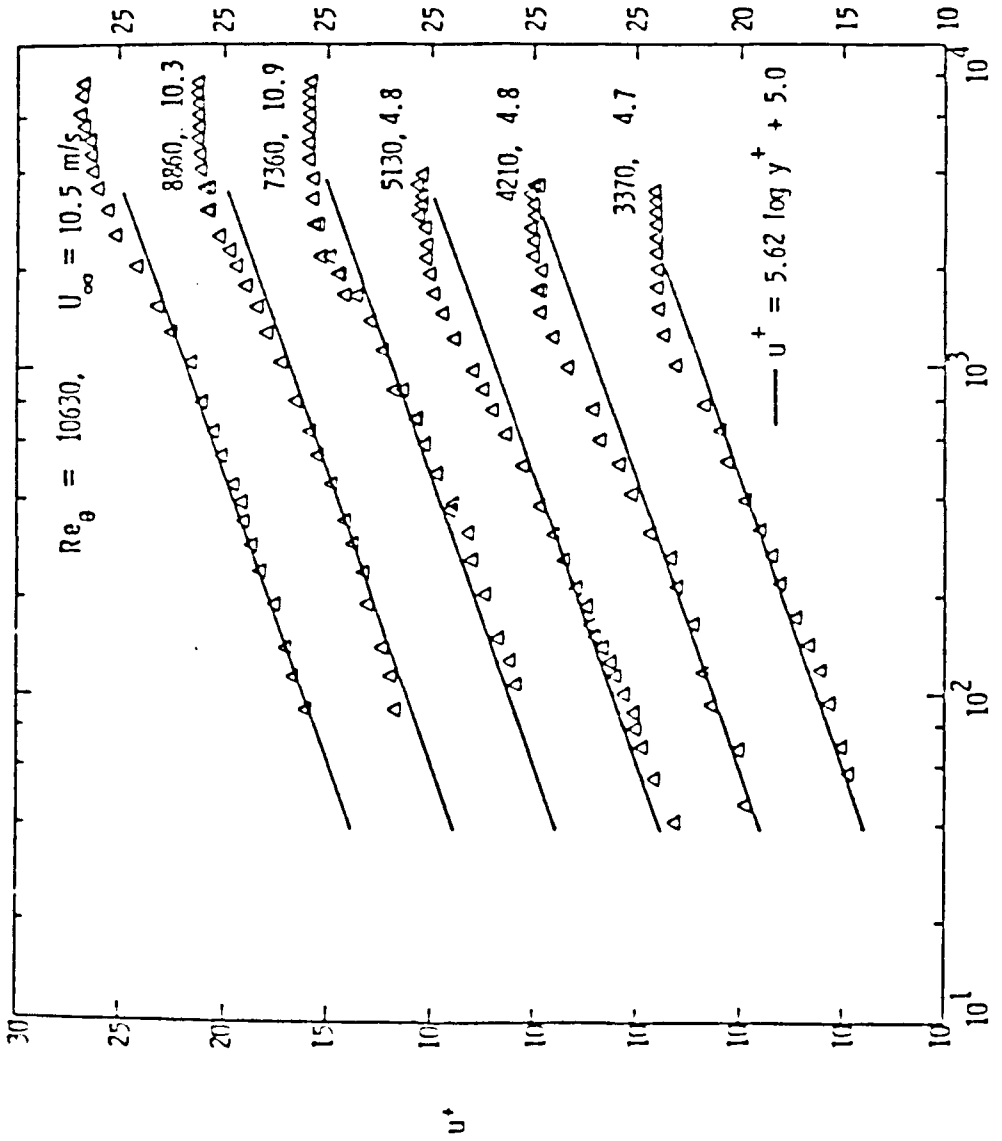

Figure 3. LDA velocity profile measurements in the undisturbed boundary layer presented in inner variables [Note shifted origins].

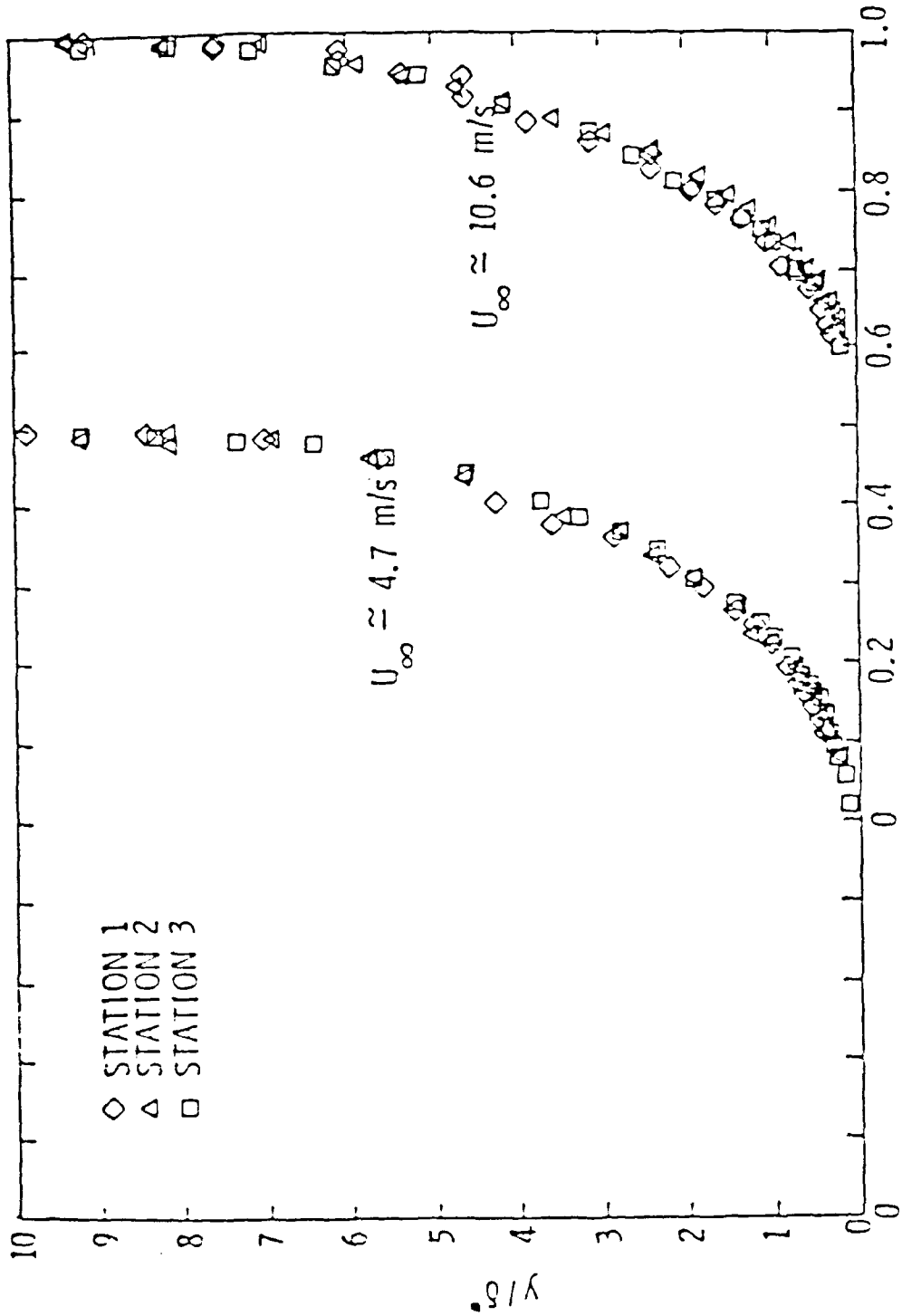

Figure 4. LDA velocity profile measurements in the undisturbed boundary layer presented in outer variables [Note shifted origins].

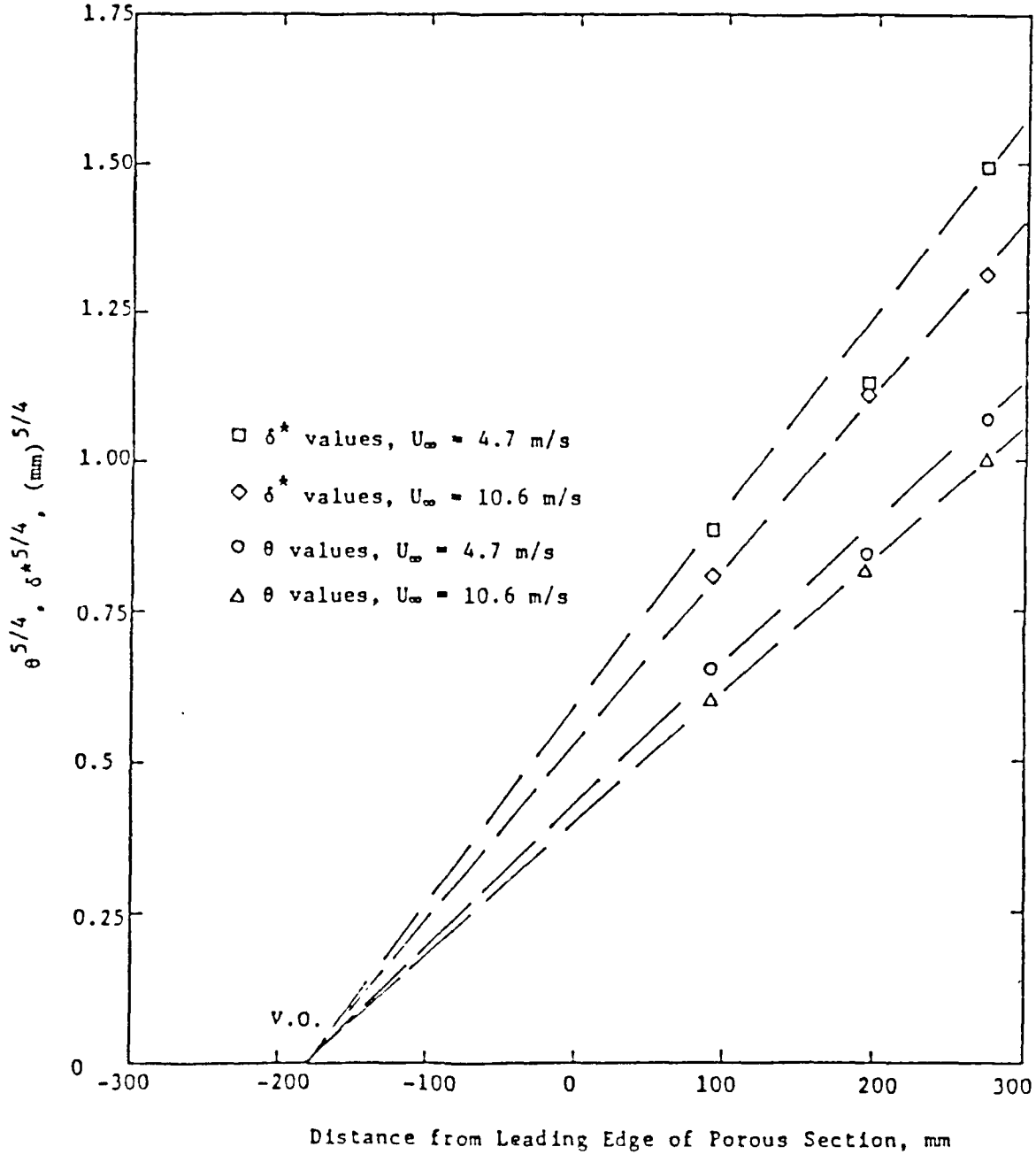

Figure 5. Determination of the virtual origin.

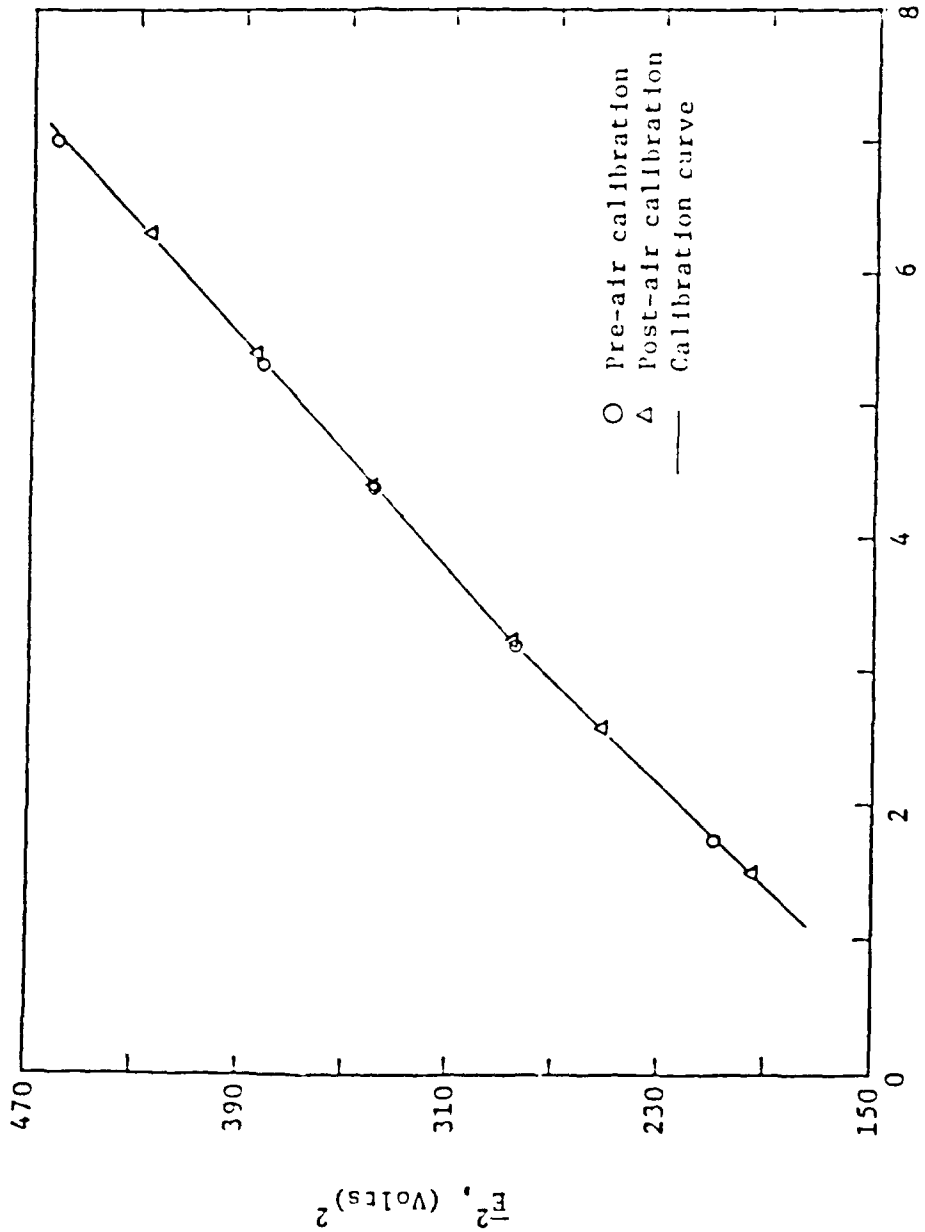

Figure 6. A typical calibration curve for the flush-mounted hot film probes.

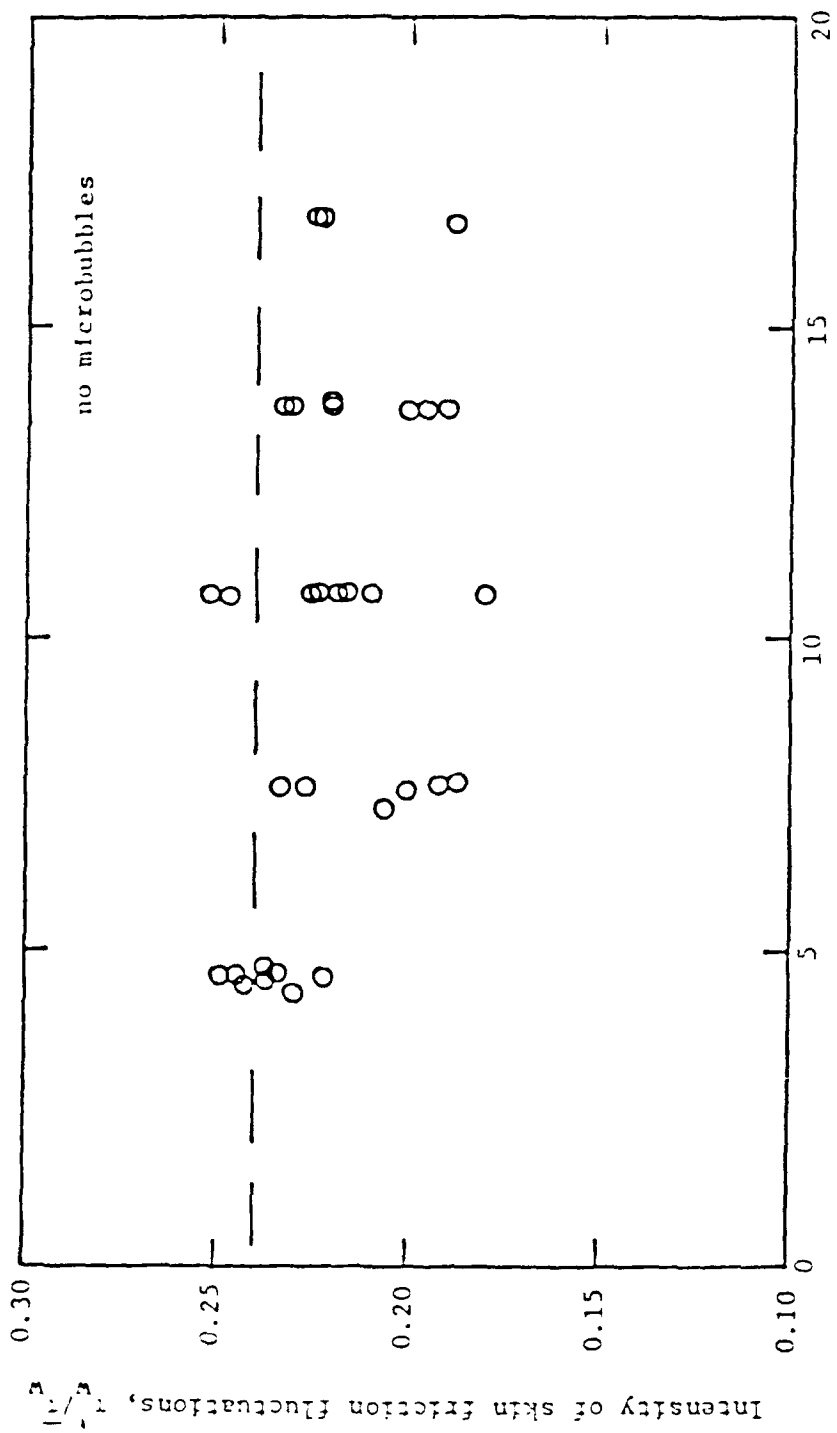

Figure 7. Hot-film measurements of the skin friction fluctuations in the undisturbed boundary layer. The Reynolds number is based on the distance of the respective probe from the virtual origin.

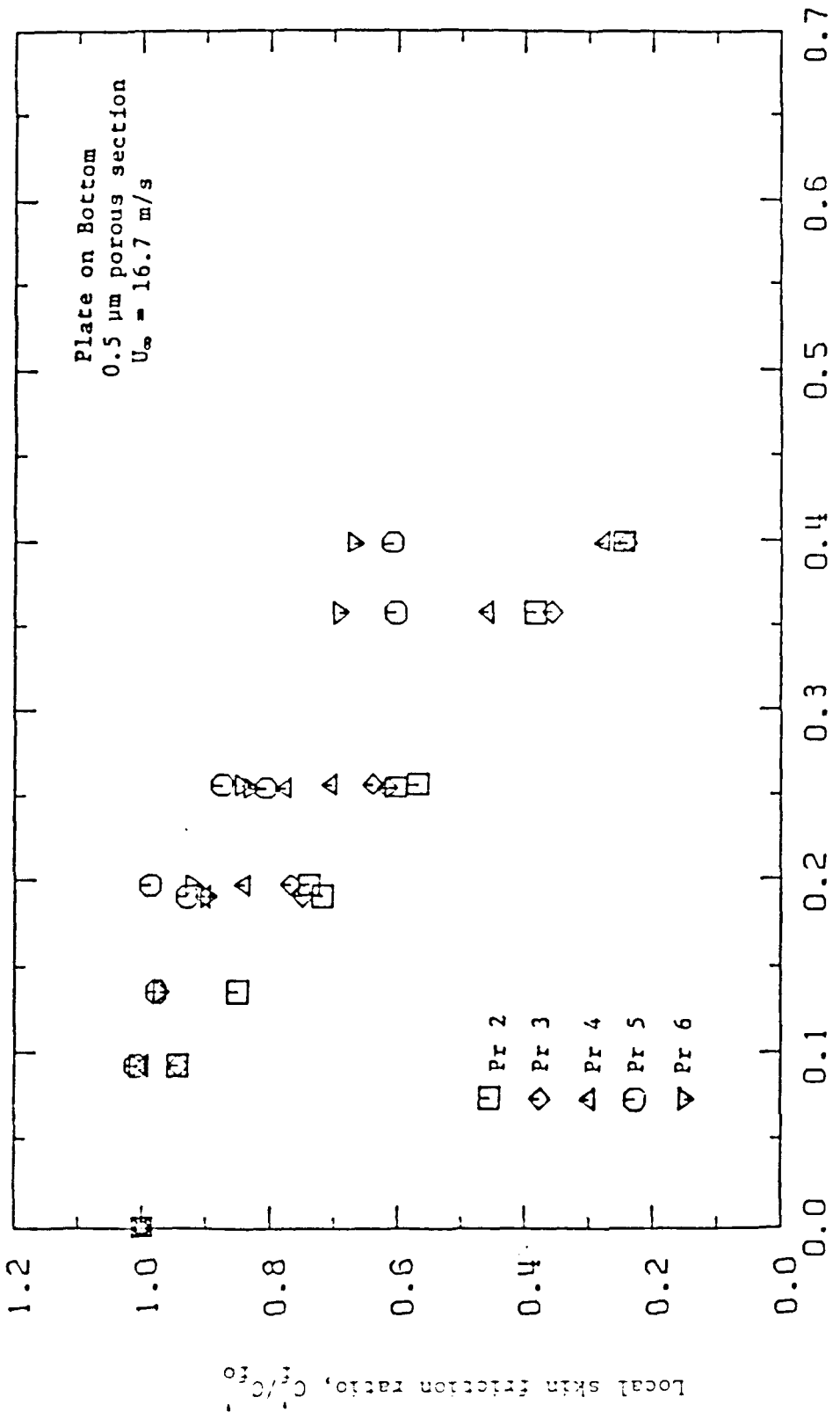

Figure 8. Hot-film measurements of the local skin friction with microbubbles as a function of the air flow rate when the plate is below the boundary layer. U_∞ = 16.7 m/s.

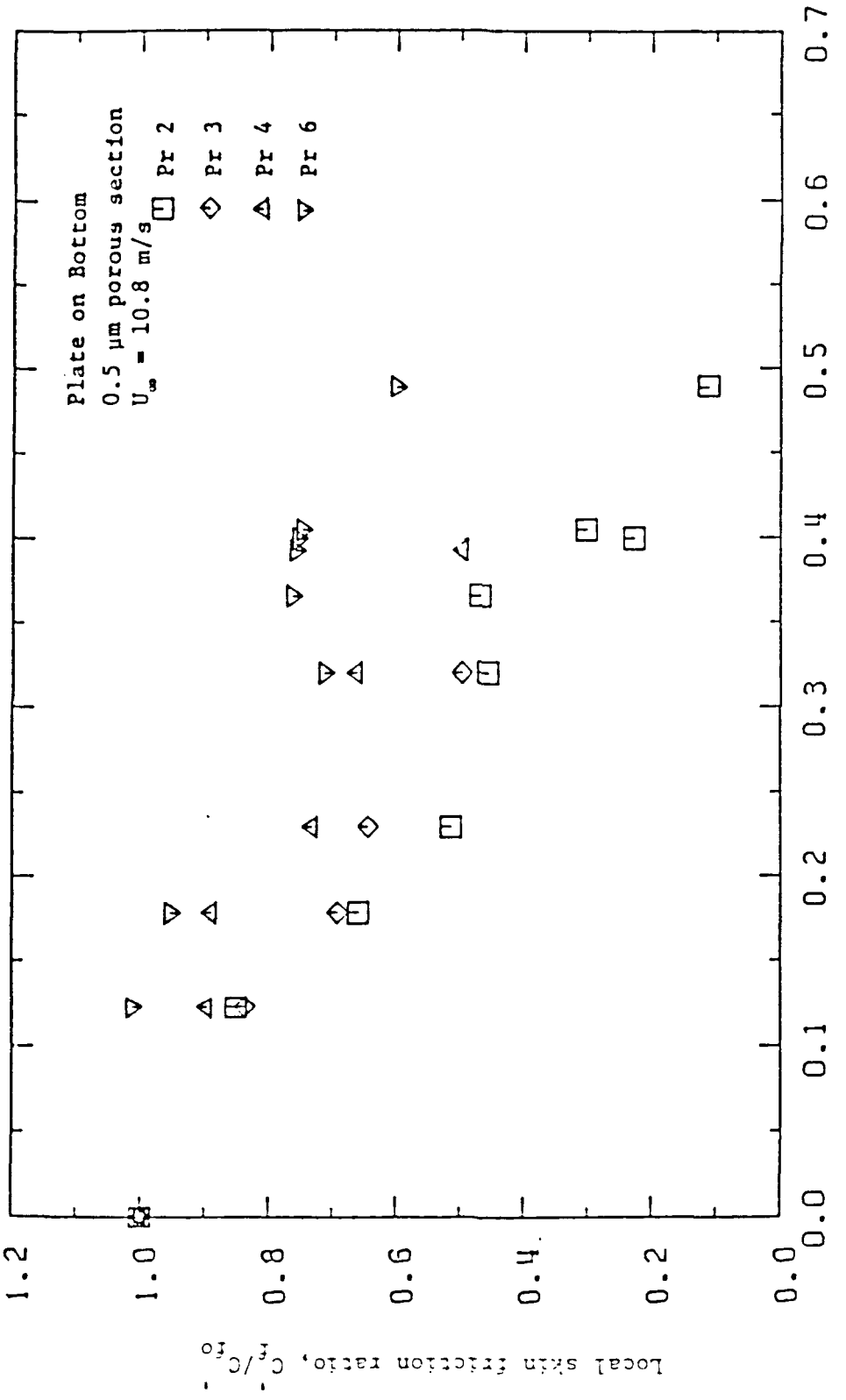

Figure 9. Hot-film measurements of the local skin friction with microbubbles as a function of the air flow rate when the plate is below the boundary layer. U_∞ = 10.8 m/s.

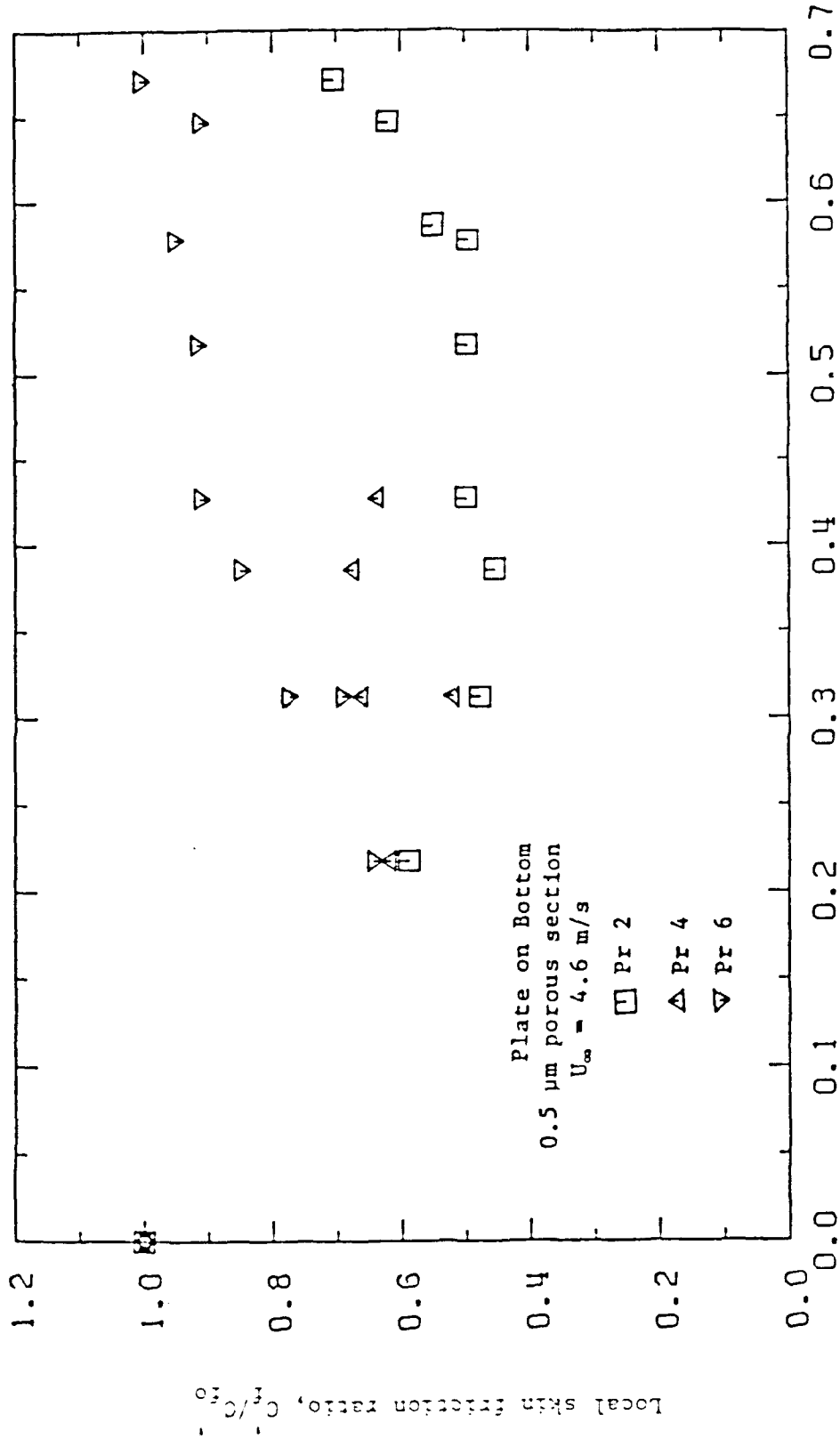

Figure 10. Hot-film measurements of the local skin friction with microbubbles as a function of the air flow rate when the plate is below the boundary layer. U_∞ = 4.6 m/s.

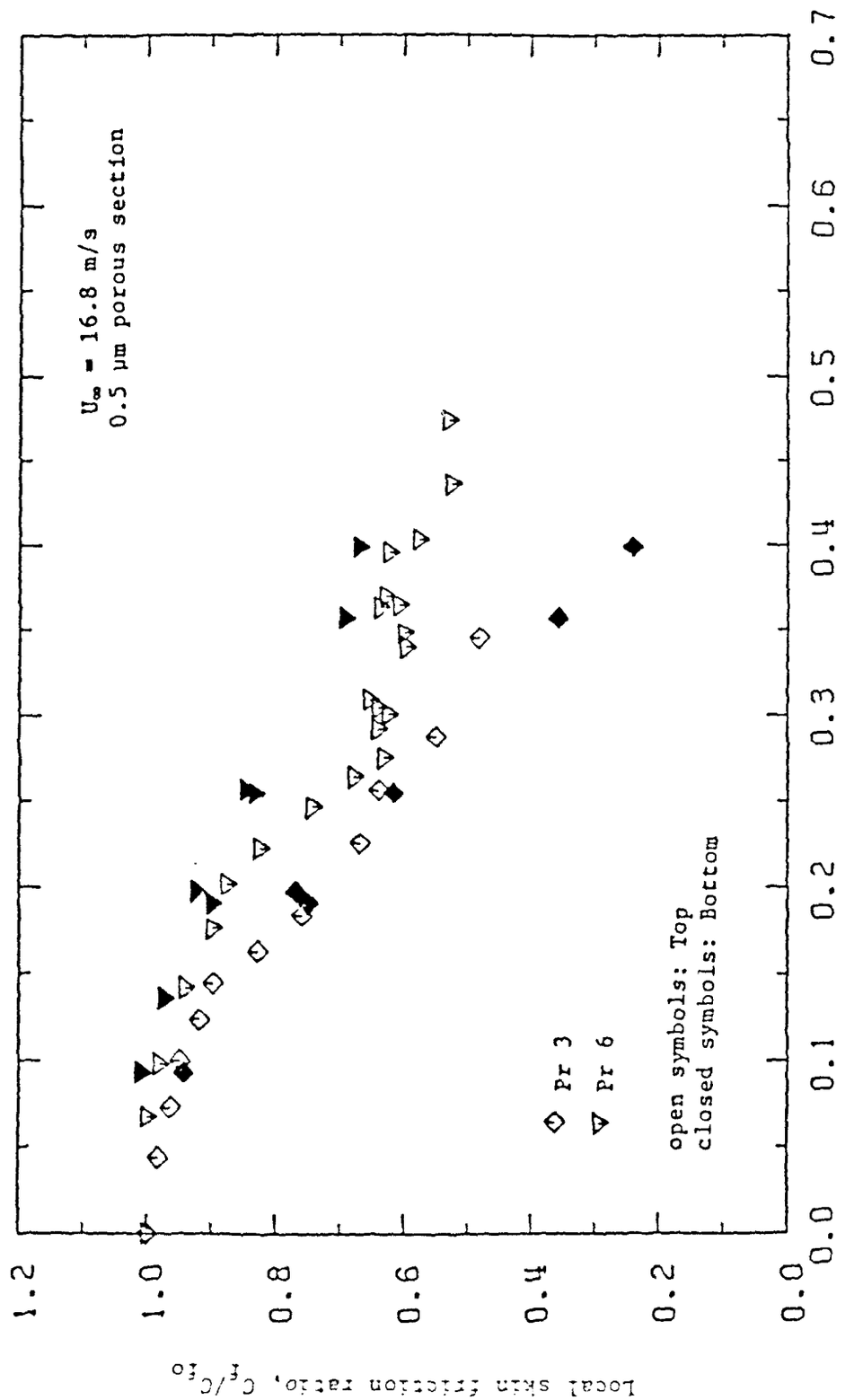

Figure 11. The effect of gravity on the hot-film measurements of the local skin friction with microbubbles. Comparison of data taken with the plate above and below the boundary layer. U_∞ = 16.8 m/s.

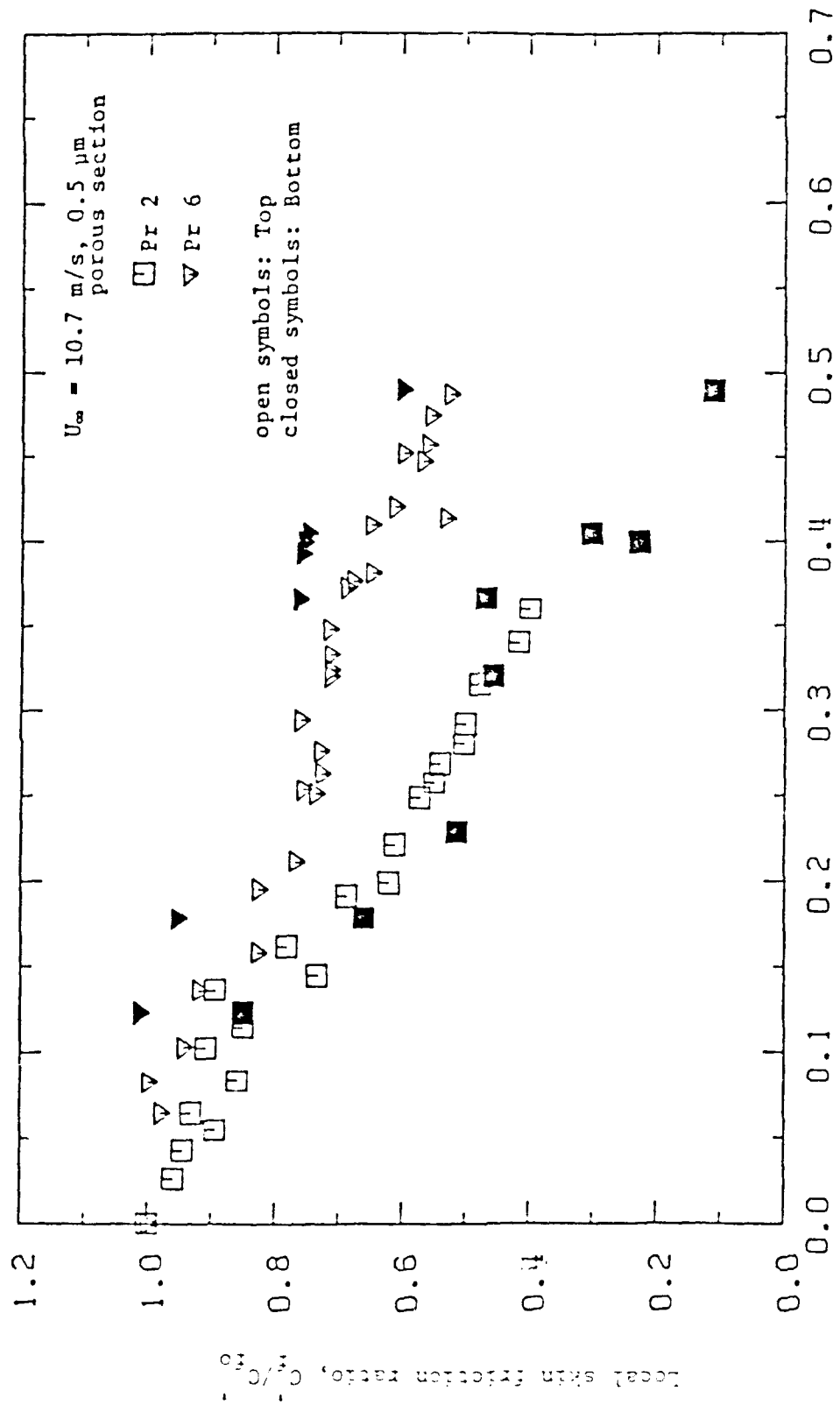

Figure 12. The effect of gravity on the hot-film measurements of the local skin friction with microbubbles. Comparison of data taken with the plate above and below the boundary layer. U_∞ = 10.7 m/s.

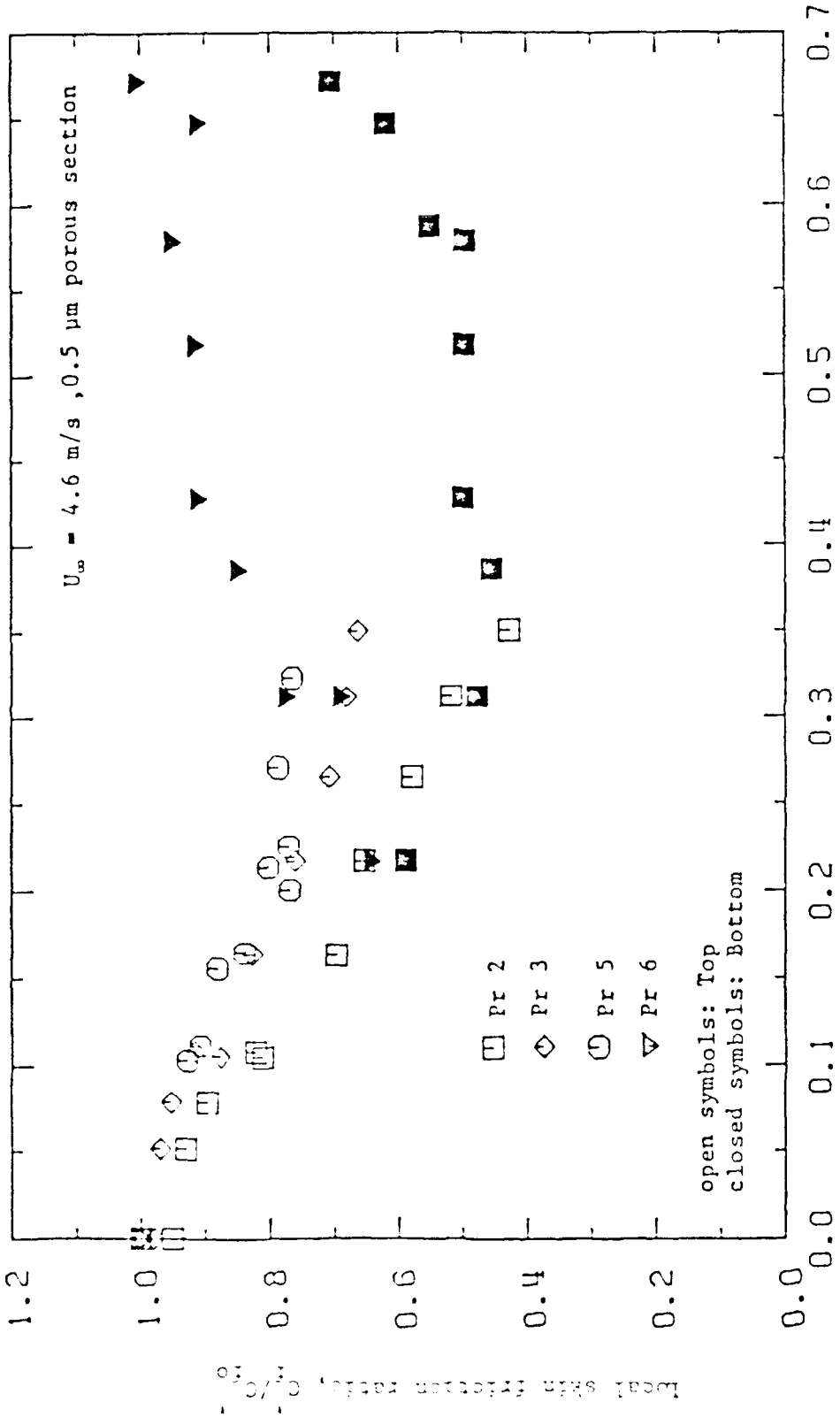

Figure 13. The effect of gravity on the hot-film measurements of the local skin friction with microbubbles. Comparison of data taken with the plate above and below the boundary layer. U_∞ = 4.6 m/s.

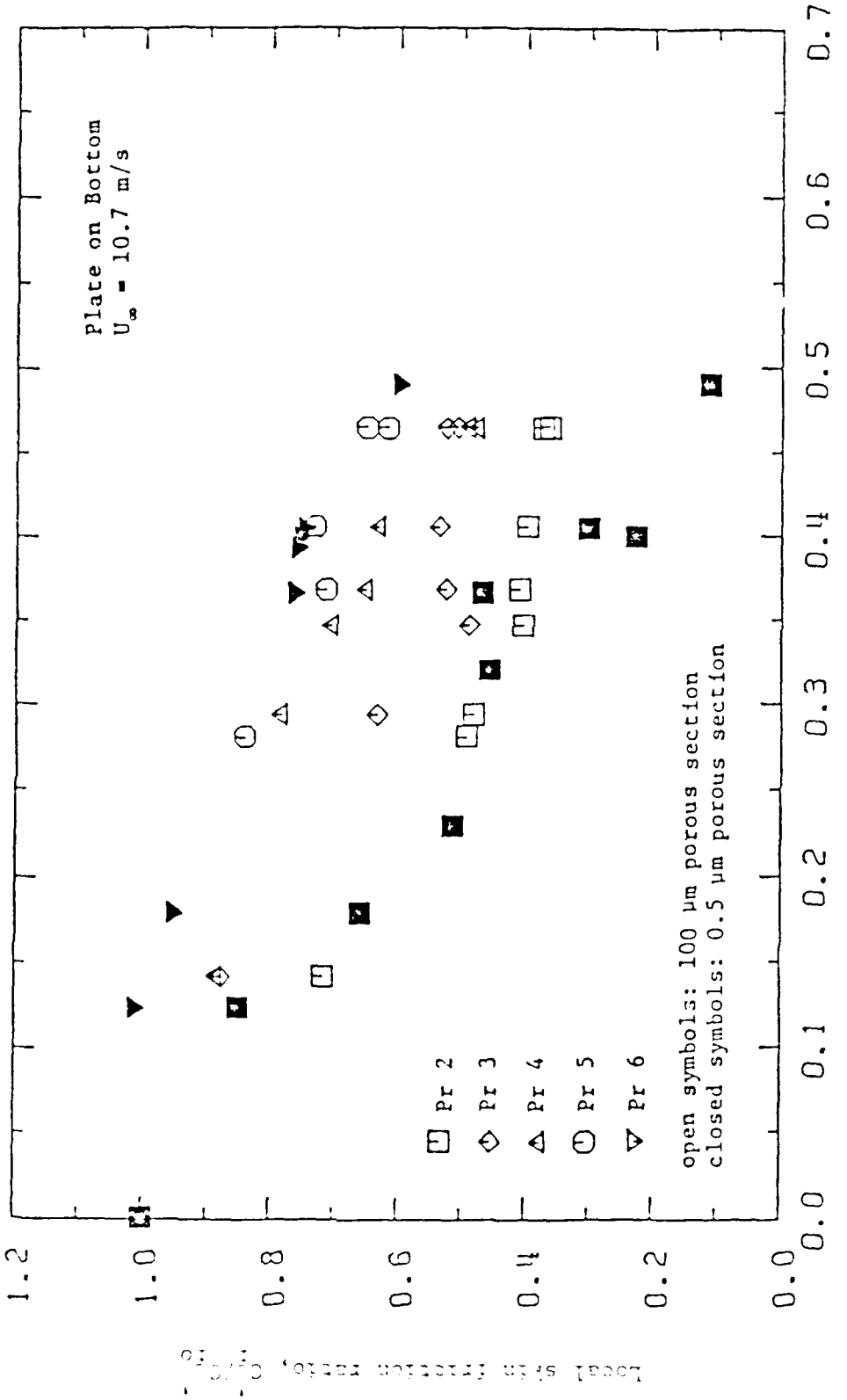

Figure 14. The effect of pore size variations on the local skin friction measurements. Comparison of data taken with the 0.5 μm and 100 μm porous sections. U_∞ = 16.8 m/s.

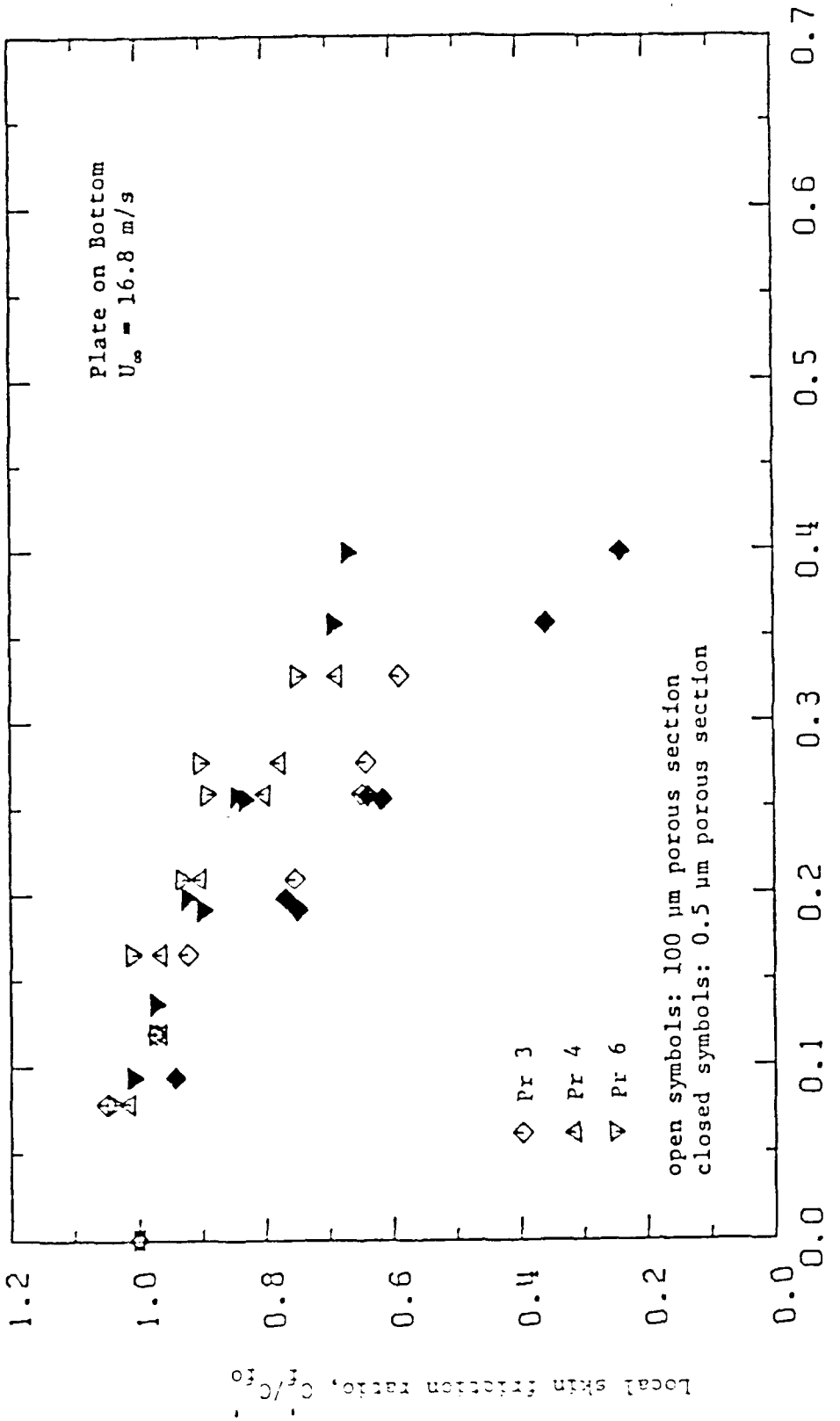

Figure 15. The effect of pore size variations on the local skin friction measurements. Comparison of data taken with the 0.5 μm and 100 μm porous sections. U_∞ = 10.7 m/s.

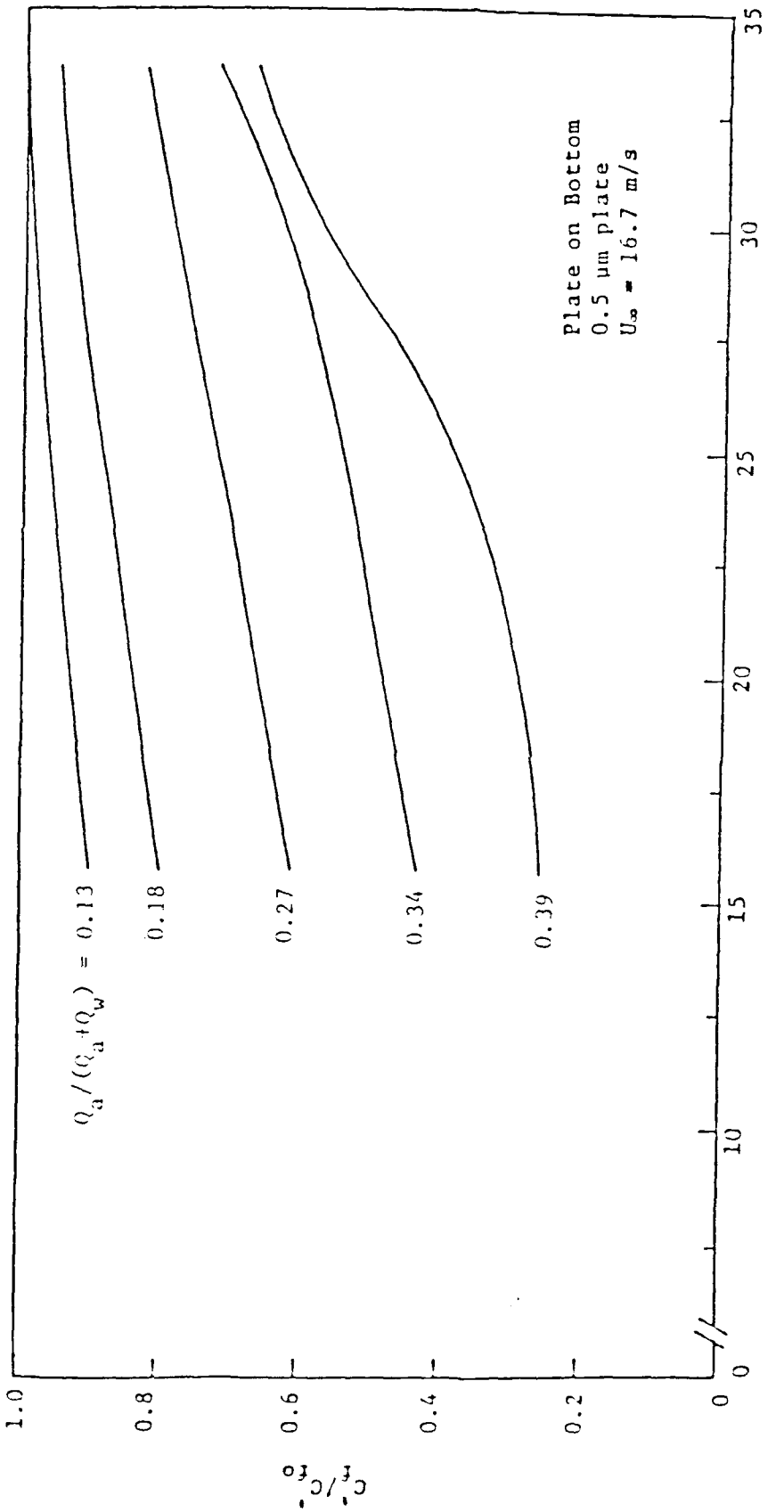

Figure 16. The downstream persistence of the skin friction reduction. The plate is below the boundary layer. U_∞ = 16.7 m/s.

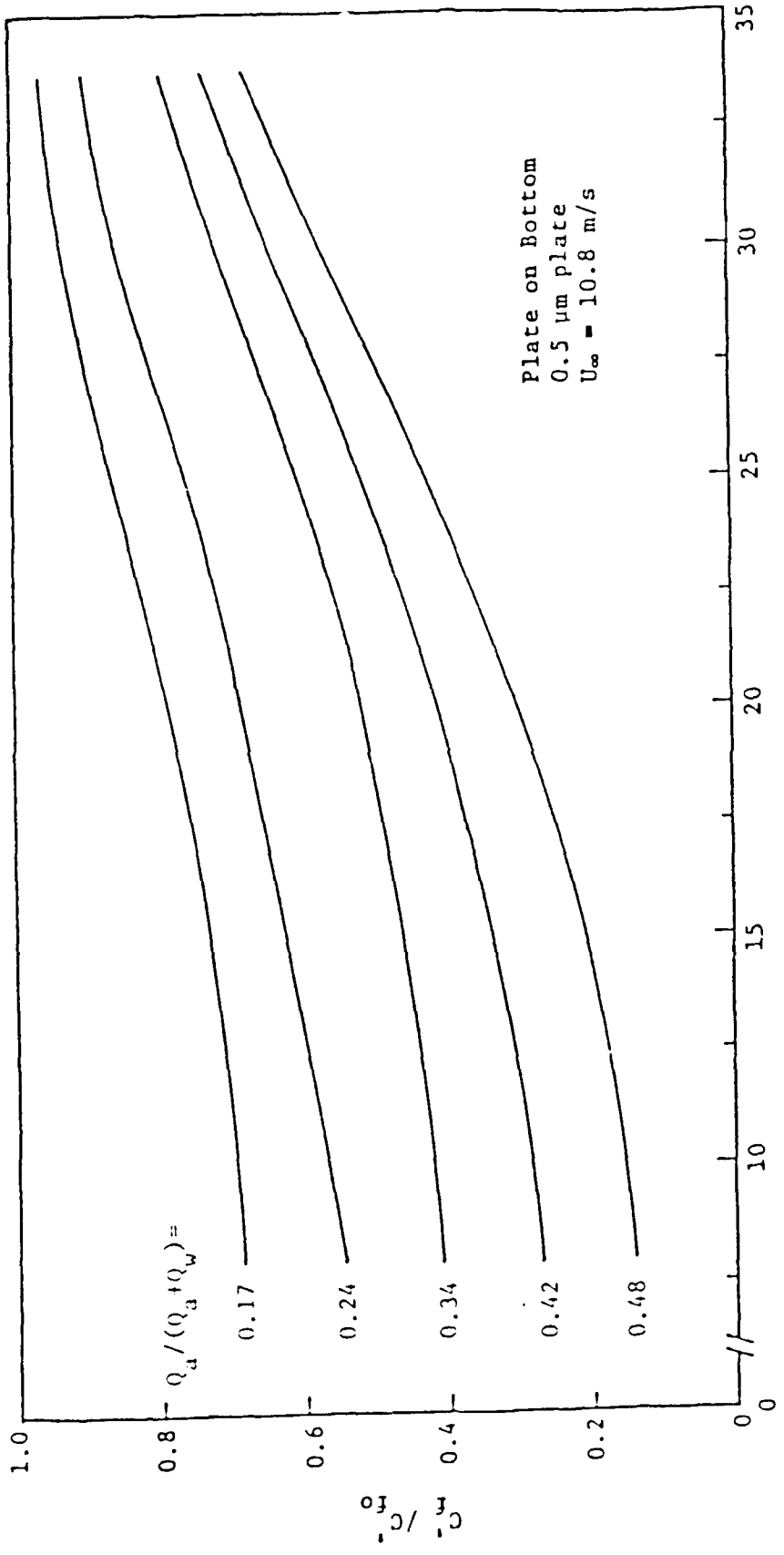

Figure 17. The downstream persistence of the skin friction reduction. The plate is below the boundary layer. U_∞ = 10.8 m/s.

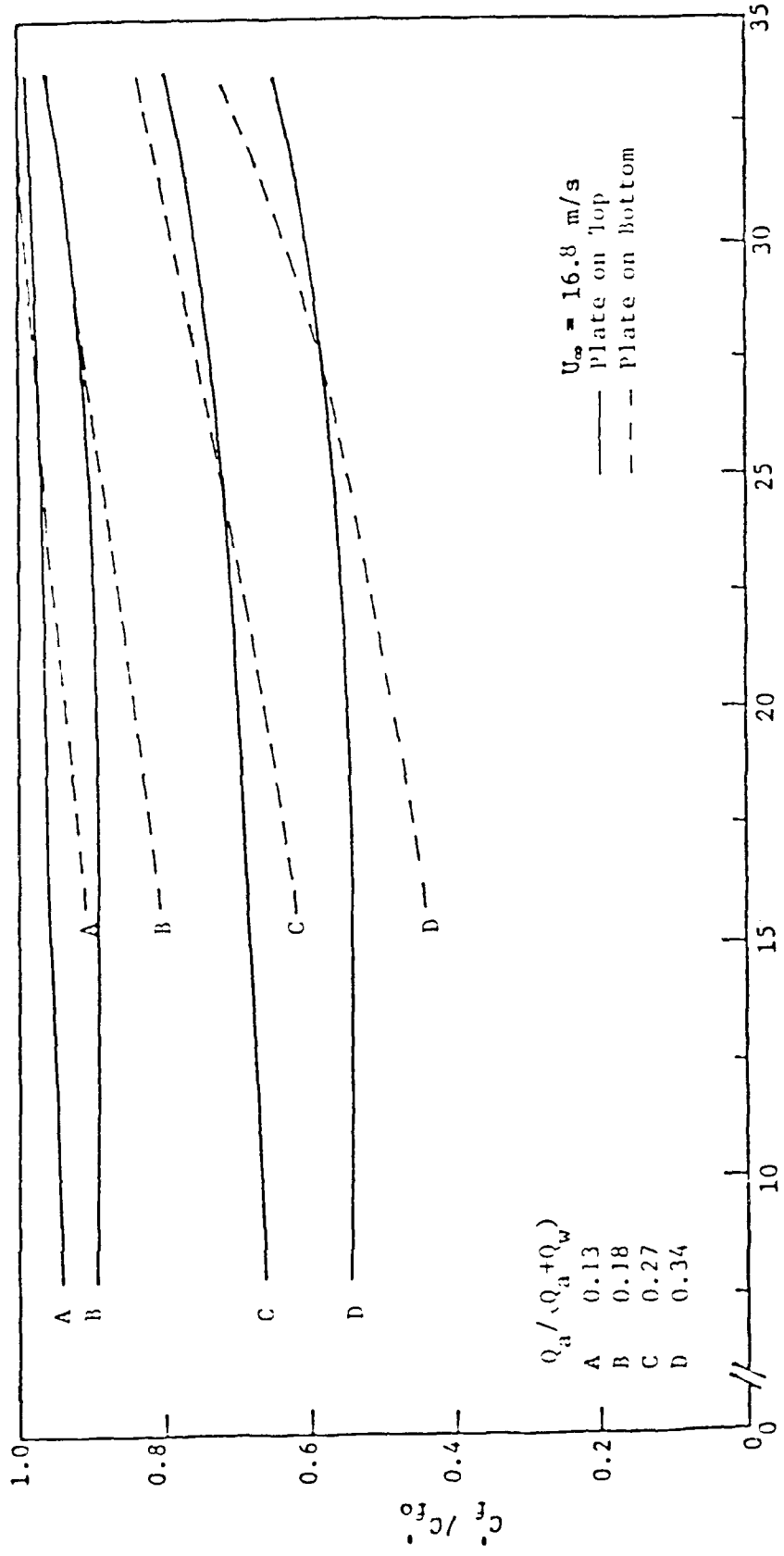

Figure 18. The downstream persistence of the skin friction reduction. Comparison of data taken with the plate above and below the boundary layer. U_∞ = 16.8 m/s.

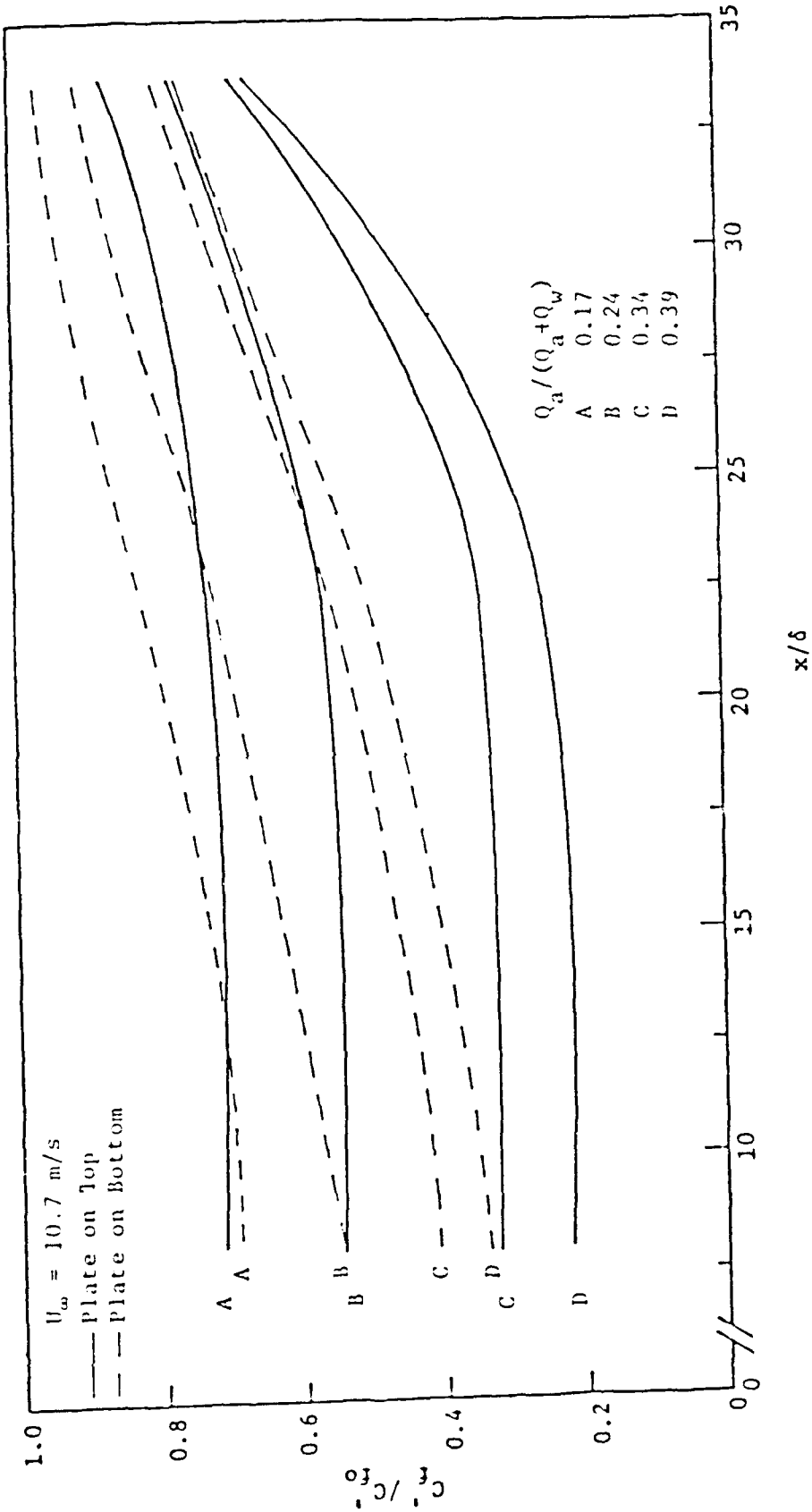

Figure 19. The downstream persistence of the skin friction reduction. Comparison of data taken with the plate above and below the boundary layer. U_∞ = 10.7 m/s.

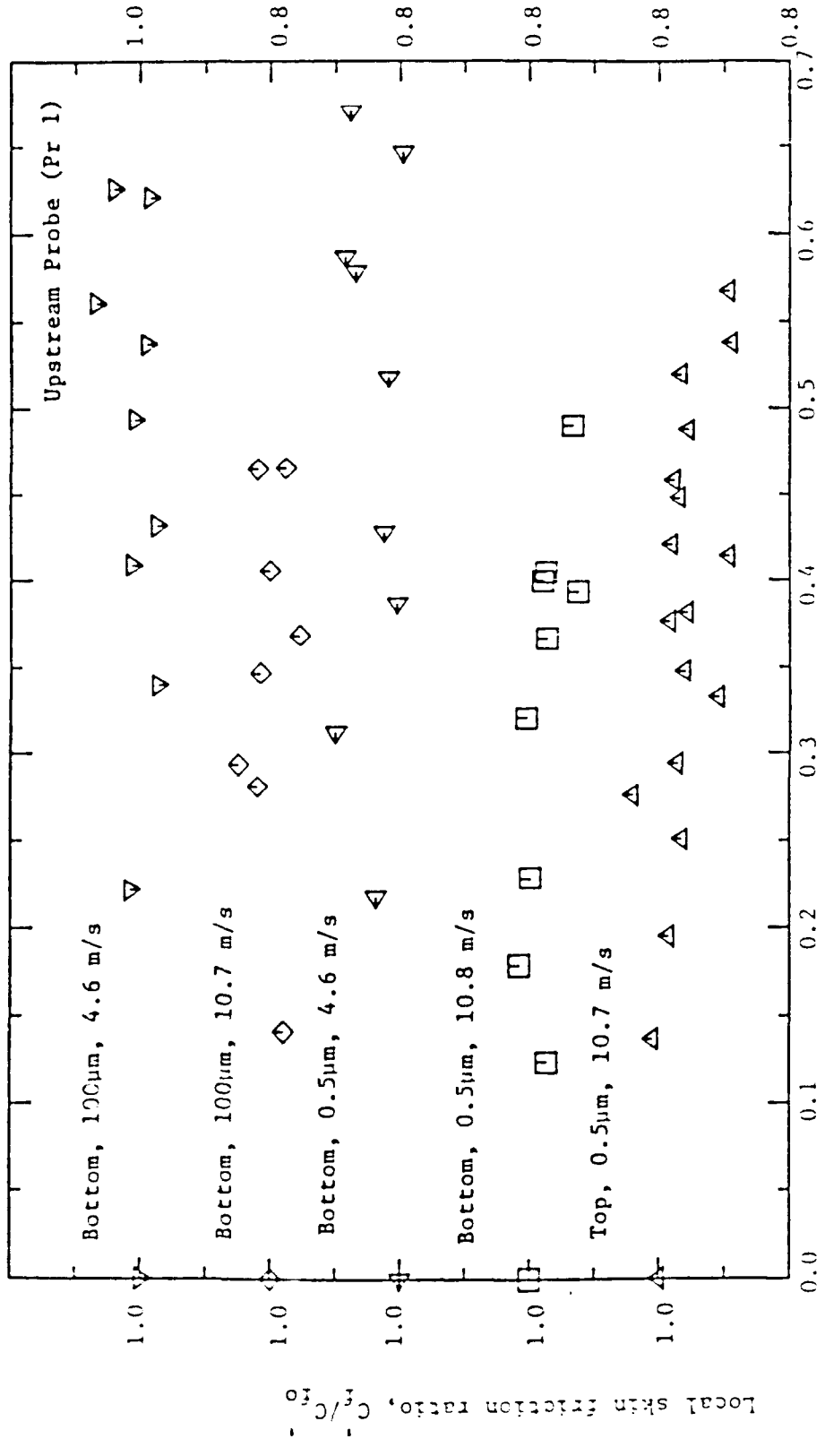

Figure 20. Hot-film measurements of the local skin friction upstream of microbubble introduction into the boundary layer [Note shifted origins].

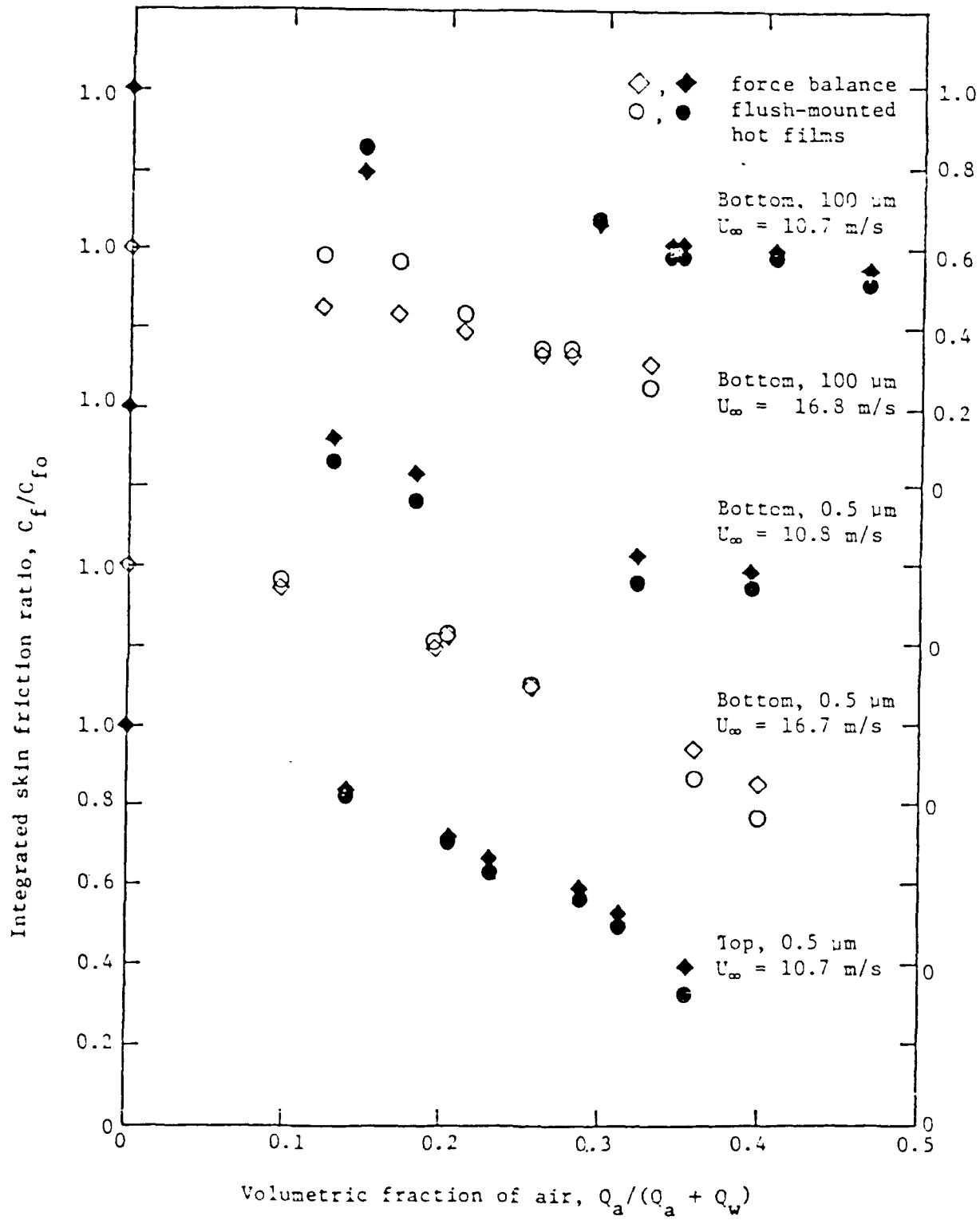

Figure 21. Comparison of the integrated skin friction reductions with microbubbles measured by the force balance with that evaluated from the hot films.

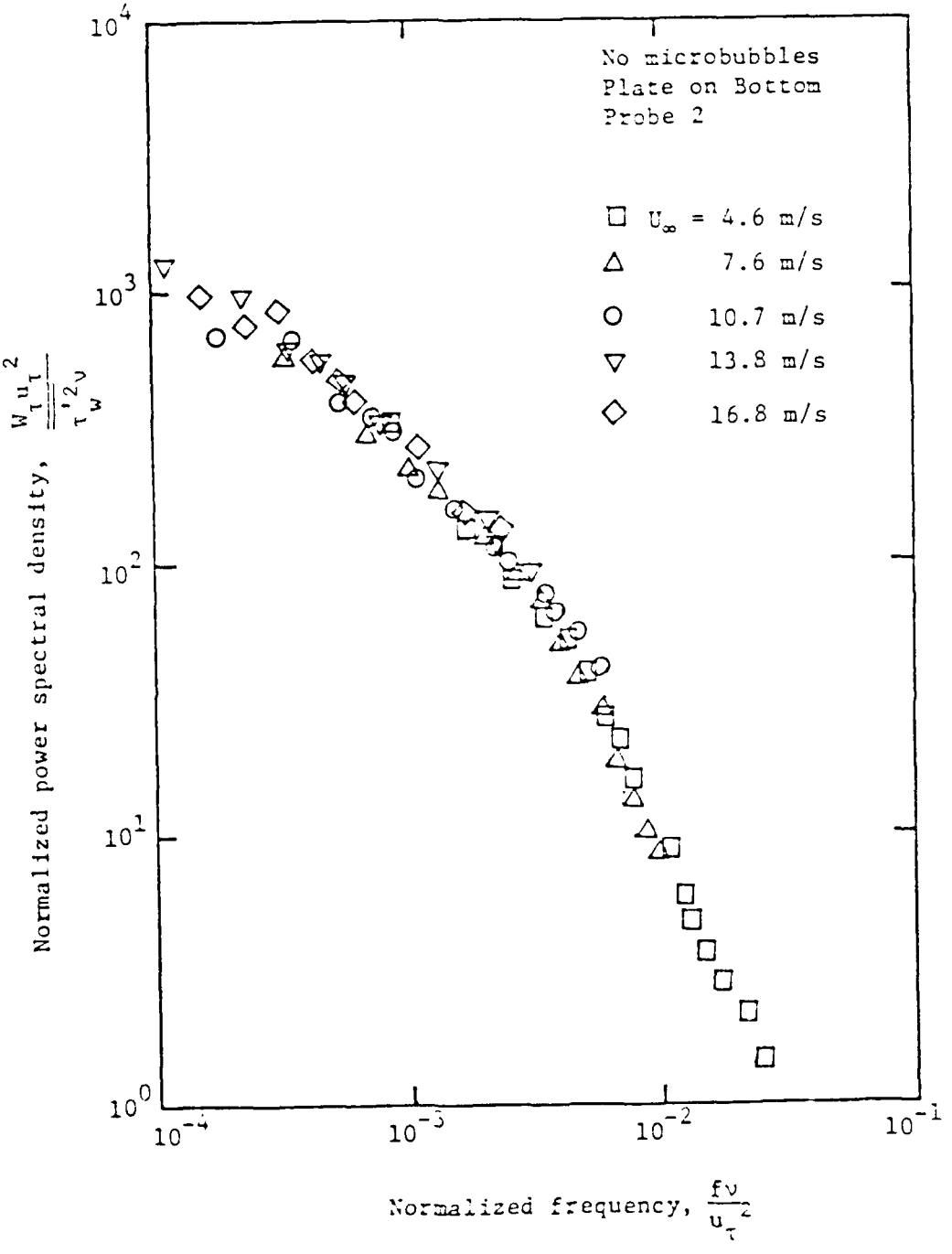

Figure 22. Normalized power spectral density functions of the hot-film signals in the presence and absence of microbubbles.

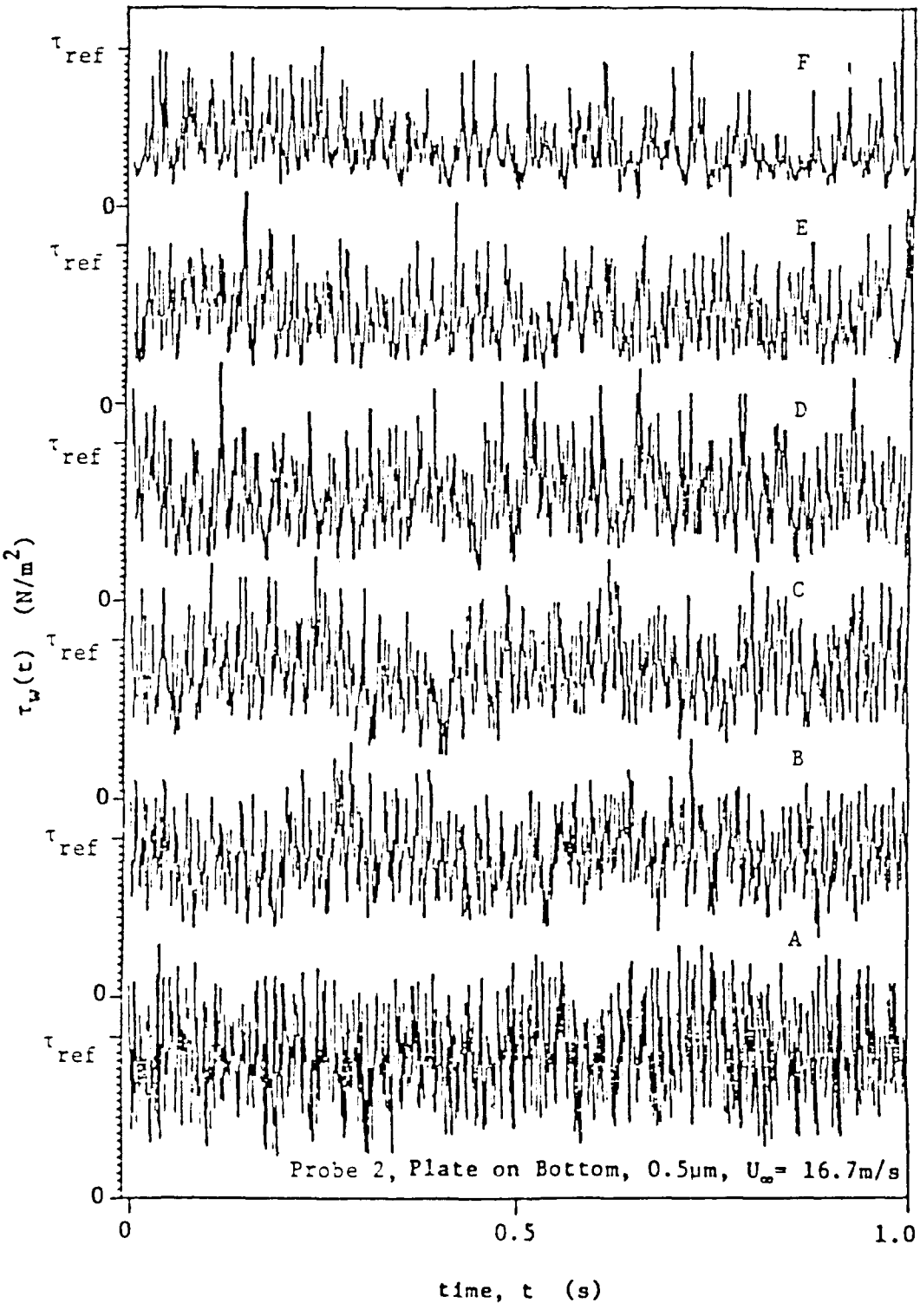

Figure 23. A sequence of linearized hot-film signal traces in the presence and absence of microbubbles. A: no microbubbles; B: 10% air, 5% C_f reduction; C: 14% air, 15% C_f reduction; D: 19% air, 28% C_f reduction; E: 26% air, 40% C_f reduction; and F: 36% air, 62% C_f reduction.

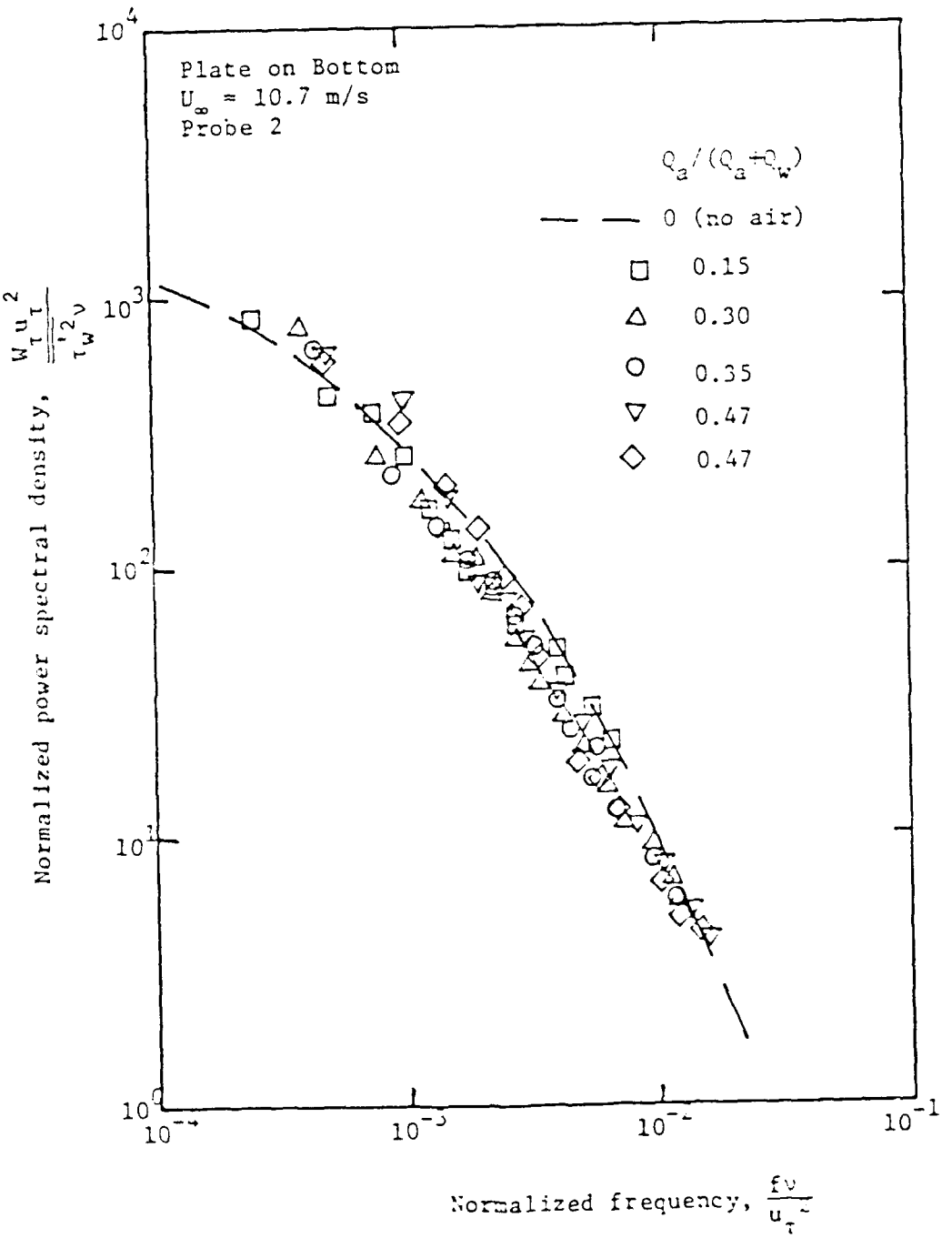

Figure 24. Normalized power spectral density functions of the hot-film signal in the presence of microbubbles. (probe 2, plate on top, 10.7 m/sec).

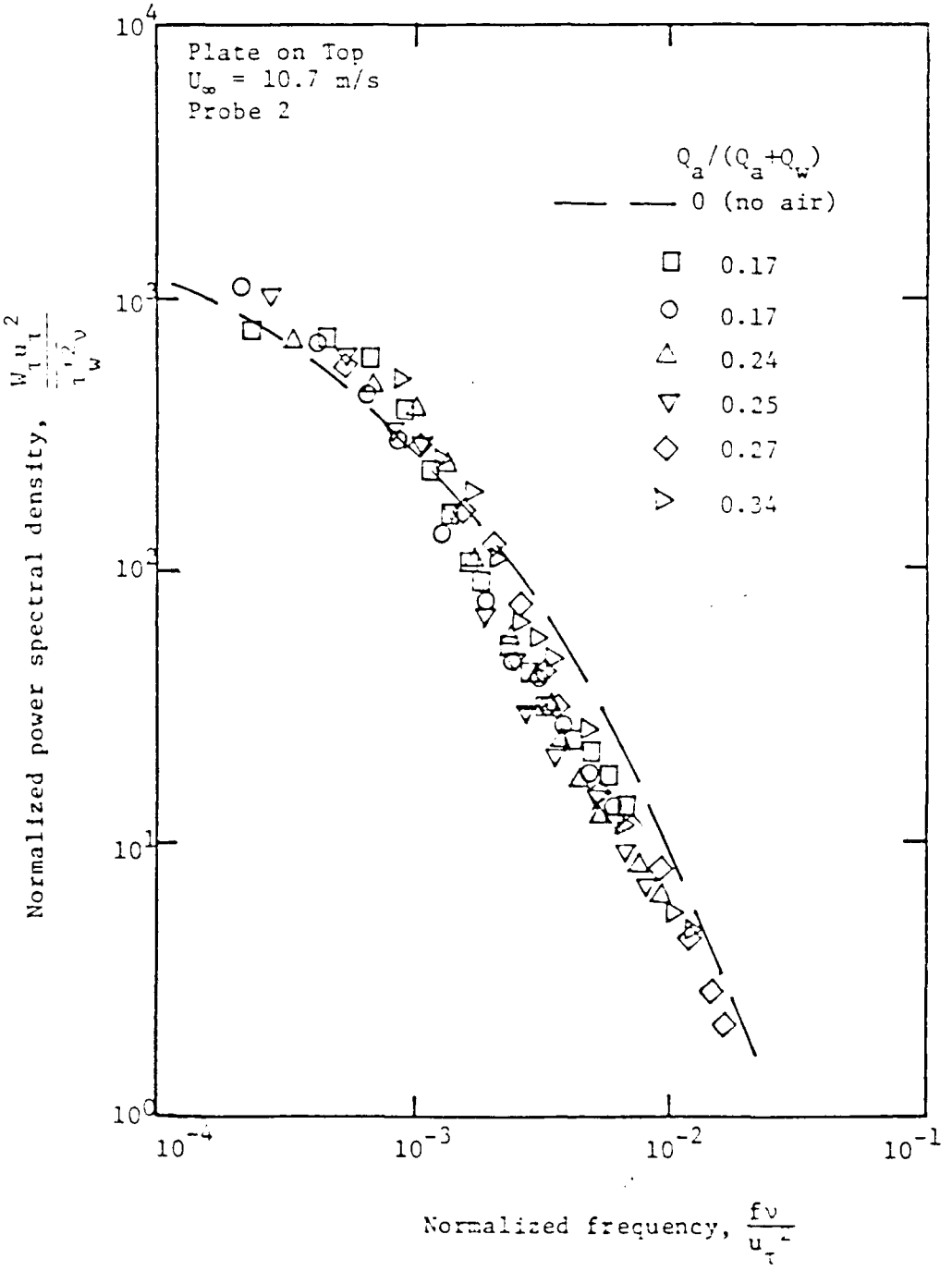

Figure 25. Normalized power spectral density functions of the hot-film signal in the presence of microbubbles. (probe 2, plate on bottom, 10.7 m/sec).

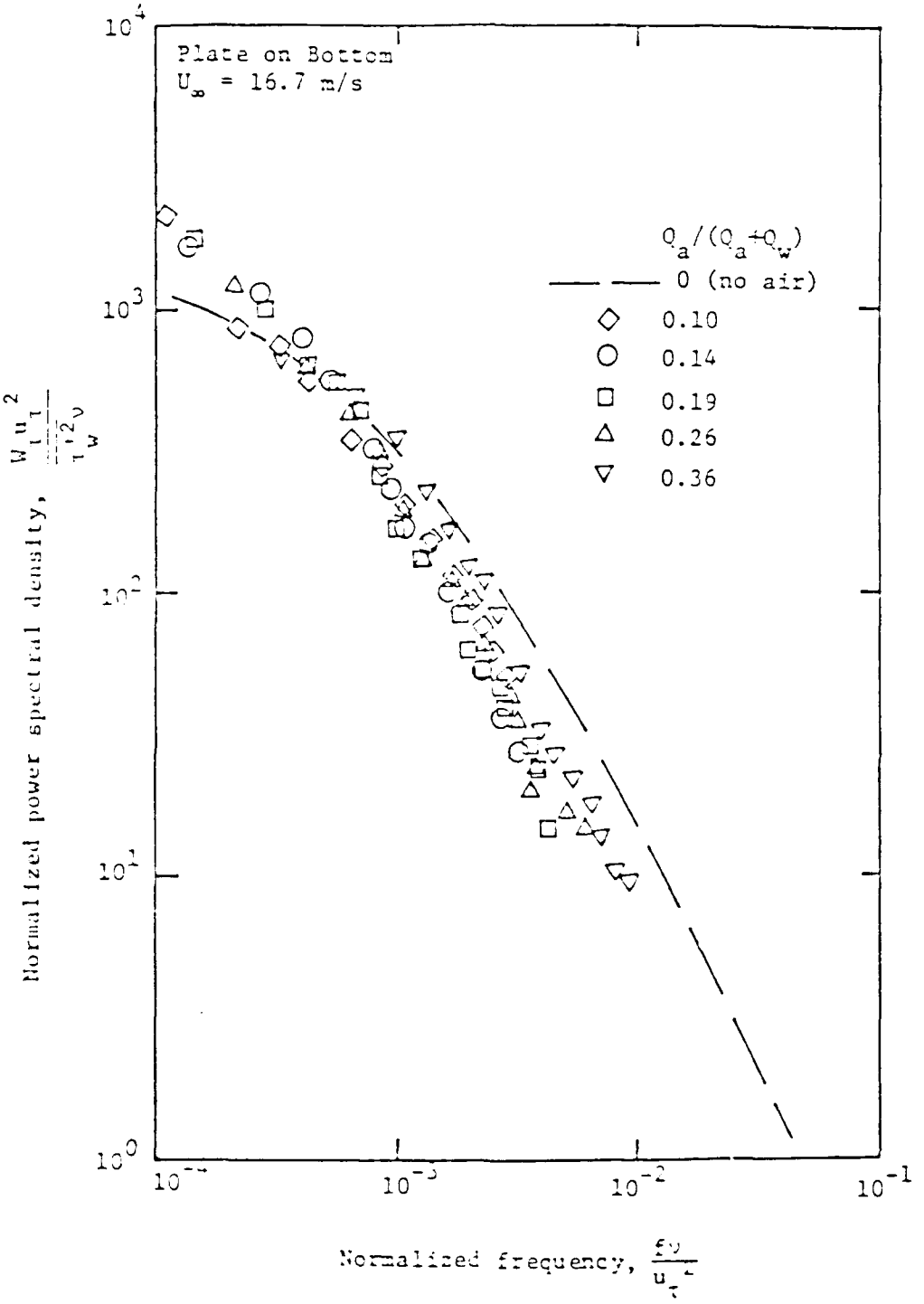

Figure 26. Normalized power spectral density functions of the hot-film signal in the presence of microbubbles. (probe 3, plate on bottom, 16.8 m/sec).

Distribution List for ARL/PSU Unclassified TM 84-136 by N. K. Madavan, S. Deutsch and C. L. Merkle, dated 24 August 1984

Commander
Naval Sea Systems Command
Department of the Navy
Washington, DC 20362
Attn: Library
Code NSEA-09G32
(Copies 1 and 2)

Commander
Naval Sea Systems Command
Department of the Navy
Washington, DC 20362
Attn: F. Romano
Code NSEA-63R
(Copy No. 3)

Commander
Naval Sea Systems Command
Department of the Navy
Washington, DC 20362
Attn: T. E. Peirce
Code NSEA-63R31
(Copy No. 4)

Commander
Naval Sea Systems Command
Department of the Navy
Washington, DC 20362
Attn: A. R. Paladino
Code NSEA-55N
(Copy No. 5)

Commander
Naval Sea Systems Command
Department of the Navy
Washington, DC 20362
Attn: W. D. Marlin
Code NSEA-931E
(Copy No. 6)

Commander
Naval Sea Systems Command
Department of the Navy
Washington, DC 20362
Attn: E. G. Liszka
Code PMS-408B
(Copy No. 7)

Commanding Officer
Naval Underwater Systems Ctr.
Department of the Navy
Newport, RI 02840
Attn: Library
Code 54
(Copy No. 8)

Commanding Officer
Naval Underwater Systems Ctr.
Department of the Navy
Newport, RI 02840
Attn: T. A. Davis
Code 36314
(Copy No. 9)

Commanding Officer
Naval Underwater Systems Ctr.
Department of the Navy
Newport, RI 02840
Attn: D. J. Goodrich
Code 3634
(Copy No. 10)

Commanding Officer
Naval Underwater Systems Ctr.
Department of the Navy
Newport, RI 02840
Attn: R. H. Nadolink
Code 3634
(Copy No. 11)

Commanding Officer
Naval Underwater Systems Ctr.
Department of the Navy
Newport, RI 02840
Attn: C. N. Pryor
Code 01
(Copy No. 12)

Commanding Officer
Naval Underwater Systems Ctr.
Department of the Navy
Newport, RI 02840
Attn: C. Hervey
Code 3634
(Copy No. 13)

Distribution List for ARL/PSU Unclassified TM 84-136 by N. K. Madavan, S. Deutsch and C. L. Merkle, dated 24 August 1984 [continuation]

Officer-in-Charge
David W. Taylor Naval Ship
Research & Development Ctr.
Department of the Navy
Bethesda, MD 20084
Attn: M. M. Sevik
Code 19
(Copy No. 14)

Officer-in-Charge
David W. Taylor Naval Ship
Research & Development Ctr.
Department of the Navy
Bethesda, MD 20084
Attn: J. H. McCarthy
Code 154
(Copy No. 15)

Officer-in-Charge
David W. Taylor Naval Ship
Research & Development Ctr.
Department of the Navy
Bethesda, MD 20084
Attn: T. T. Huang
Code 1552
(Copy No. 16)

Officer-in-Charge
David W. Taylor Naval Ship
Research & Development Ctr.
Department of the Navy
Bethesda, MD 20084
Attn: J. Shen
Code 194
(Copy No. 17)

Commander
Naval Surface Weapons Ctr.
Department of the Navy
Silver Spring, MD 20910
Attn: G. C. Gualaurd
(Copy No. 18)

Office of Naval Research
800 North Quincy Street
Department of the Navy
Arlington, VA 22217
Attn: R. Whitehead
Code 432
(Copy No. 19)

Office of Naval Research
800 North Quincy Street
Department of the Navy
Arlington, VA 22217
Attn: M. M. Reischman
Code 432F
(Copy No. 20)

Mr. P. S. Klebanoff
National Bureau of Standards
771.FM105
Washington, DC 20234
(Copy No. 21)

Mr. J. M. McMichael
National Bureau of Standards
771.FM105
Washington, DC 20234
(Copy No. 22)

Mr. R. J. Hansen
Naval Research Laboratory
Department of the Navy
Washington, DC 20390
(Copy No. 23)

Mr. R. King
Rand Corporation
1700 Main Street
Santa Monica, CA 90406
(Copy No. 24)

Mr. J. Aroesty
Rand Corporation
1700 Main Street
Santa Monica, CA 90406
(Copy No. 25)

Mr. C. Gazley
Rand Corporation
1700 Main Street
Santa Monica, CA 90406
(Copy No. 26)

Mr. A. R. Wazzan
Rand Corporation
1700 Main Street
Santa Monica, CA 90406
(Copy No. 27)

Distribution List for ARL/PSU Unclassified TM 84-136 by N. K. Madavan, S. Deutsch and C. L. Merkle, dated 24 August 1984 [continuation]

Mr. W. W. Haigh
Dynamics Technology, Inc.
22939 Hawthorne Blvd.
Torrance, CA 90505
(Copy No. 28)

Mr. G. L. Donohue
Dynamics Technology, Inc.
22939 Hawthorne Blvd.
Torrance, CA 90505
(Copy No. 29)

Prof. W. M. Phillips
Chairman
Dept. of Mech. Engr.
Purdue University
Lafayette, IN 47907
(Copy No. 30)

Dr. R. F. Mons
Westinghouse Electric Corp.
Post Office Box 1458
Annapolis, MD 21404
(Copy No. 31)

Prof. J. L. Lumley
Sibley School of Engineering
Cornell University
Ithaca, NY 14850
(Copy No. 32)

Prof. C. L. Merkle
Dept. of Mech. Engineering
The Pennsylvania State University
University Park, PA 16802
(Copy No. 33)

Mr. N. K. Madavan
Dept. of Mech. Engineering
The Pennsylvania State University
University Park, PA 16802
(Copy No. 34)

Director
Applied Research Laboratory
The Pennsylvania State University
Post Office Box 30
State College, PA 16804
Attn: ARL/PSU Library
(Copy No. 35)

Director
Applied Research Laboratory
The Pennsylvania State University
Post Office Box 30
State College, PA 16804
Attn: S. Deutsch
(Copies 36 through 38)

Director
Applied Research Laboratory
The Pennsylvania State University
Post Office Box 30
State College, PA 16804
Attn: G. B. Gurney
(Copy No. 39)

Director
Applied Research Laboratory
The Pennsylvania State University
Post Office Box 30
State College, PA 16804
Attn: R. E. Henderson
(Copy No. 40)

Director
Applied Research Laboratory
The Pennsylvania State University
Post Office Box 30
State College, PA 16804
Attn: L. R. Hettche
(Copy No. 41)

Director
Applied Research Laboratory
The Pennsylvania State University
Post Office Box 30
State College, PA 16804
Attn: B. R. Parkin
(Copy No. 42)

Director
Applied Research Laboratory
The Pennsylvania State University
Post Office Box 30
State College, PA 16804
Attn: GTWT Files
(Copy No. 43)